

CONTAINMENT BUILDING LINER CORROSION—CORROSION AND LEAK RATE MODELS

Prepared for

**U.S. Nuclear Regulatory Commission
Contract NRC-HQ-12-C-04-0069**

Prepared by

**Osvaldo Pensado¹
Pavan Shukla¹
Kaushik Das¹
Todd Mintz¹
Roberto Pabalan¹
Stuart Stothoff¹
Alberto Sagüés²**

**¹Center for Nuclear Waste Regulatory Analyses
San Antonio, Texas**

**²University of South Florida
Department of Civil and Environmental Engineering
Tampa, Florida**

July 2013

ABSTRACT

This report analyzes corrosion of the steel liner of nuclear power plant containment buildings initiated at the steel and concrete interface due to the presence of debris, predominantly wood. This report expands on work by an expert panel previously convened by NRC to evaluate a number of operational events. The expert panel concluded that wood left behind during construction of the containment building and abutting the containment liner could cause corrosion by a macrocell process. The expert panel report included approximate calculations of corrosion rates. Therefore, the purpose of the present report was to develop a more refined modeling approach to identify physical parameters that affect the corrosion process. The scenario for a loss-of-coolant accident (LOCA) in a containment with a breached liner was evaluated to determine how corrosion could affect containment leakage.

For macrocell corrosion, one important parameter controlling corrosion rates and the extent of damage is the concrete ionic resistivity. A reasonable value for the resistivity consistent with observations of through-wall liner corrosion is on the order of 10 k Ω -cm. In this range of concrete resistivity, other physical variables, such as oxygen diffusion through concrete, kinetic rates of oxygen reduction and iron passive dissolution, and the amount of rebar embedded in the concrete, play a secondary role in determining corrosion rates and the extent of damage. These physical parameters would play a more important role if the resistivity of concrete was of a larger magnitude.

A synthesis model was built to calculate the area of the corrosion damage as function of the localized corrosion rate, concrete resistivity, and macrocell driving potential. The corrosion rate was estimated as a function of pH based on simulations using the OLIAnalyzer Studio® software (OLISystems, Inc., 2013). Estimates of the corrosion area were computed assuming large but reasonable values of the macrocell driving potential. Results indicated that corrosion areas ranging from a few to a few tens of square centimeters are possible. The analysis disregarded limitations imposed by the contact area between the wood and the steel liner. It is unlikely for the corrosion damage to extend far beyond the area of contact because (i) tight contact is required to keep the local porewater chemically different (i.e., low pH) from the bulk alkaline concrete porewater chemistry, and (ii) propagation of an acidic porewater front, involving diffusion of hydrogen ions and reaction with hydroxides in concrete, is a very slow process. More realistic computations accounting for limited contact would result in smaller estimates of corrosion areas. Also, consideration of smaller values of the driving potential would reduce the corrosion area estimates. There is uncertainty in the carbon steel corrosion rates as function of both pH and the electric potential in concrete porewater solutions, with pH lowered by the presence of wood. A Monte Carlo model was implemented to output a range of liner corrosion areas to be used as input to leak rate estimates, conditional on model assumptions.

A model was developed to compute leak rates of gas (water vapor and air) in a LOCA scenario with a steel liner breached by through-wall corrosion. The model was based on mass and energy balance equations, and ideal gas relations. The flow pathway was postulated originate at the hole in the liner and follow the gap between the liner and the containment wall until leaking to the outside atmosphere through an existing containment penetration. The size of the gap between the liner and containment wall was referred to as the effective aperture. Other pathways such as gas flow through the concrete or gas flow in through-wall cracks were not considered in this analysis. The model was implemented as a Monte Carlo model to allow for propagation of uncertainty in inputs, such as the area of the liner corrosion damage. Results from an integrated leak test performed in a containment building with a breached liner were

used to calibrate the model. Comparable results to the plant leak rate test were obtained if the effective aperture was 0.1 mm [3.9 mil] or less. Leak rates scaled in proportion to the cube of the aperture. Sensitivity analyses indicated that other parameters, such as the length or width of the flow pathway, had less effect on the leak rates. The size of the breached area had a strong effect on the calculated leakage rate only when this area was small, for example less than 1 cm² [0.15 in²]. Under the assumption of impermeable concrete, if the aperture is less than 0.01 mm [0.39 mil], the leak rate from the containment building is negligible. Containment liner corrosion is likely to be associated with a small aperture because a low pH solution can only be established in a tight space, and because the volume from iron corrosion products will press into the containment wall.

REFERENCE

OLISystems, Inc. "OLIAnalyzer Studio®." Morris Plains, New Jersey: OLISystems, Inc. 2013. <<http://www.olisystems.com/new-streamanalyzer.shtml>> (March 18, 2013).

CONTENTS

	Page
Section	Page
ABSTRACT	ii
FIGURES	v
TABLES	vi
ACKNOWLEDGMENTS	vii
1 INTRODUCTION.....	1-1
1.1 Background	1-1
1.2 Inspection Requirements.....	1-2
1.3 Expert Panel Summary	1-3
1.4 Objectives.....	1-3
1.5 Report Organization	1-4
2 CORROSION MODEL	2-1
2.1 Approach	2-1
2.2 Macrocell Corrosion Background	2-2
2.3 Model Description.....	2-3
2.4 Model Implementation	2-6
2.5 Sensitivity Analysis on the Net Current	2-9
2.6 Limiting Case: Disc Electrode with an Infinite Counter Electrode at a Far Distance	2-16
2.7 Thermodynamic and Corrosion Analysis.....	2-17
2.8 Estimates of Corrosion Damage Areas	2-21
2.9 Discussion—Corrosion Model	2-29
3 LEAK RATE MODEL.....	3-1
3.1 Approach	3-1
3.2 Mass and Energy Balance Model.....	3-1
3.3 Gas Flow Through Compartment B.....	3-5
3.4 Comparison to Leak Tests	3-9
3.5 Sensitivity Analyses.....	3-11
3.6 Discussion—Leak Rate Model	3-17
4 CONCLUSIONS	4-1
5 REFERENCES.....	5-1

APPENDIX—ALTERNATIVE OXYGEN REDUCTION EQUATIONS

FIGURES

Figure	Page
2-1 Schematic Representation of the Macrocell Corrosion Process for the Liner and Concrete Containment System	2-2
2-2 Example of Finite Element Mesh to Numerically Solve the Differential Equations.....	2-7
2-3 Example Distribution of the Solution Potential (Contours Forming Approximate Circles) and Current Lines (Lines Emanating From the Anode).....	2-8
2-4 Effect of the Anode Potential on the Oxygen Distribution	2-10
2-5 Example of Potential and Oxygen Distribution Obtained With a High Value of Oxygen Diffusion Coefficient.....	2-11
2-6 Net Ionic Current Versus Driving Potential.....	2-13
2-7 Net Ionic Current Versus Driving Potential.....	2-14
2-8 Variation of the Net Current As Function of the Driving Potential and Model Parameters.....	2-15
2-9 Comparison of the Disk Electrode Systems to the Macrocell Corrosion Model of Liner and Rebar System	2-16
2-10 pH of Cement Pore Solutions As a Function of CH ₃ COOH Concentration (Weight%) Calculated Using OLIAnalyzer Studio (OLYSystems, Inc., 2013).....	2-19
2-11 Calculated Current Density and Corrosion Rate of Iron in Concrete As Functions of Electrode Potential and pH	2-20
2-12 Assumed Cumulative Distribution for the Concrete Ionic Resistivity	2-22
2-13 Numerical Distribution of the Driving Potential Derived With Monte Carlo Analysis	2-23
2-14 Estimates of Corrosion Damage Area From the Monte Carlo Analysis	2-25
2-15 Estimates of Corrosion Damage Area From the Monte Carlo Analysis	2-26
2-16 Combined Distribution for the Corrosion Area from the Monte Carlo Analysis	2-27
2-17 Conceptualized Stages in the Propagation of a Corrosion Front Leading to Through-Wall Corrosion	2-28
3-1 Schematic of a Pressurized Water Reactor Containment Building	3-2
3-2 Four Compartment Concept for the Mass and Energy Balance Model.....	3-2
3-3 Example Pressure and Temperature Transients Considered in Analysis of Containment Response Following a Loss-of-Coolant Accident	3-3
3-4 Geometrical Abstraction of the Diffusive Pathway	3-7
3-5 Grid Structure Used to Numerically Solve the Gas Flow Equation	3-8
3-6 Pressure As a Function of Time and Position	3-10
3-7 Fractional Release and Cumulative Leak as Functions of Time and the Aperture, <i>a</i>	3-10
3-8 Fractional Release As a Function Model Parameters	3-12
3-9 Fractional Release As a Function of Aperture	3-14
3-10 Average Pressure (From 500 Monte Carlo Realizations) As a Function of Time and Position	3-15
3-11 Sensitivity Analysis on the Fractional Release Including Variation in the Aperture.....	3-16

TABLES

Table	Page
1-1 Incidences of Through-Wall Corrosion on Containment Liner at U.S. Nuclear Power Plants	1-1
2-1 Parameter Values Considered in the Parametric Studies.....	2-12
2-2 Summary of Measured Cement Pore Solution Composition (Moles/Liter) in Published Literature	2-18
2-3 Cement Pore Solution Composition (Moles/Liter) Used in Corrosion Analysis	2-19
3-1 Description of Fractional Release Symbols	3-4
3-2 Central Values of Models Parameters Used for Results in Figure 3-7	3-13
3-3 Distributions and Values of Model Parameters for Monte Carlo Leak Rate Computations	3-13

ACKNOWLEDGMENTS

The Center for Nuclear Waste Regulatory Analyses (CNWRA[®]) prepared this report to document work performed for the U.S. Nuclear Regulatory Commission (NRC) under Contract No. NRC-HQ-12-C-04-0069. The activities reported here were performed on behalf of the NRC Office of Nuclear Regulatory Research. This report is an independent product of CNWRA and does not necessarily reflect the views or regulatory position of NRC.

The authors gratefully acknowledge discussions with G. Wittmeyer and G. Walter to develop a gas flow model, and with Leonardo Cáseres on macrocell corrosion and concrete properties. The feedback provided by G. Oberson, D. Dunn, and P. Klein of NRC was very valuable to guide the work. The support by A. Nordquist to set up and run simulations in the COMSOL software is recognized. Finally, the authors acknowledge G. Walter, Y.M. Pan, and E. Pearcy for their technical and programmatic reviews and B. Street for her administrative support.

QUALITY OF DATA, ANALYSES, AND CODE DEVELOPMENT

DATA: All CNWRA-generated data contained in this report meet quality assurance requirements described in the Geosciences and Engineering Division Quality Assurance Manual. Sources of other data should be consulted for determining the level of quality of those data.

ANALYSES AND CODES: The OLIAnalyzer Studio[®] Version 3.0 software (OLISystems, Inc., 2013) was used to compute polarization curves of iron in concrete porewater. COMSOL Multiphysics[®] Version 4.3a (COMSOL, Inc., 2013) was employed to solve differential equations for mass and charge balance. OLIAnalyzer Studio Version 3.0 and COMSOL Multiphysics are controlled under Technical Operating Procedure (TOP)-18. Commercial software not controlled under TOP-18 was used for other multiple computations, and it is listed as follows. Mathematica[®] Version 8 (Wolfram Research, 2013) was used for general data analysis and plotting. GoldSim Version 10.5 (GoldSim Technology Group, LLC., 2013) was used to build Monte Carlo models for the corrosion damage area on the liner and leak rate computations.

REFERENCES

COMSOL, Inc. “COMSOL Multiphysics.” Burlington, Massachusetts: COMSOL, Inc. 2013. <<http://www.comsol.com/>> (March 8, 2013).

GoldSim Technology Group, LLC. “GoldSim Version 10.5.” Issaquah, Washington: GoldSim Technology Group, LLC. 2013. <<http://www.goldsim.com/Home/>> (March 11, 2013).

OLISystems, Inc. “OLIAnalyzer Studio.” Morris Plains, New Jersey: OLISystems, Inc. 2013. <<http://www.olisystems.com/new-streamanalyzer.shtml>> (March 18, 2013).

Wolfram Research. “Mathematica Version 8.” Champaign, Illinois: Wolfram Research. 2013. <<http://www.wolfram.com/>> (March 15, 2013).

1 INTRODUCTION

1.1 Background

As of 2011, there were 104 nuclear power plants licensed to operate in the United States. Of these, 66 plants have containment buildings constructed with an inner steel liner plate in contact with a concrete shell that is a few feet thick. The steel liner in contact with the concrete shell is nominally 6 to 10 mm [0.25 to 0.375 in] thick and is designed in conjunction with the concrete containment building to function as an essentially leak-tight barrier that prevents the release of radioactive materials under accident conditions. Through-wall corrosion of the containment liner has been observed at various U.S. nuclear power plants. The operating experience incidents of through-wall corrosion are summarized in Table 1-1 (Dunn, et al., 2011). Between 1999 and 2009, four instances of containment liner corrosion were identified in U.S. plants where the corrosion initiated at the concrete and steel interface (listed in Table 1-1).

Table 1-1. Incidences of Through-Wall Corrosion on Containment Liner at U.S. Nuclear Power Plants*

Incident	Finding
In May 1999, at Brunswick Unit 2, three through-wall penetrations were identified	A worker's glove was found at one through-wall penetration site.
In September 1999 at North Anna Unit 2, a through-wall penetration was discovered on a rusted section of a liner plate	A through wall hole was discovered with a 0.635-cm [0.25-in] diameter. A small piece of wood was embedded on concrete. The size of the wood piece was 10 cm × 10 cm × 1.8 m [3.9 in × 3.9 in × 5.9 ft].
In March 2001, at DC Cook Unit 2, a small hole was discovered in the liner plate that was believed to be manmade; however, some external corrosion of the liner also occurred	A through-wall hole, 1.9-cm [0.75-in] diameter at interior surface, 0.47-cm [0.185-in] diameter at the liner and concrete interface, was discovered. The wooden handle portion of a wire brush was found at the concrete liner interface.
In June 2009, at Beaver Valley Unit 1, a through wall hole was discovered	A piece of wood of dimensions 5 cm × 10 cm × 15 cm [1.97 in × 3.94 in × 5.9 in] was found embedded in the concrete. Another through-wall penetration caused by an embedded piece of wood was found at a rectangular hole size 2.5 cm × 1.0 cm [0.98 in × 0.394 in].

*Dunn, D.S, A.L. Pulvirenti, and M.A. Hiser. "Containment Liner Corrosion Operating Experience Summary: Technical Letter Report–Revision 1." ML112070867. Washington, DC: U.S. Nuclear Regulatory Commission. 2011.

Another instance of liner corrosion was noted at Beaver Valley Unit 1 in March 2006 during replacement of steam generators. The containment concrete was hydro-blasted to create room for the steam generator. Both general and localized corrosion at the liner and concrete interface was discovered after the liner was exposed (after hydro-blasting of the concrete). Although it cannot be confirmed that localized corrosion observed at the liner and concrete interface was due to a foreign object, it is conjectured that foreign material may have been embedded in the concrete during construction and was destroyed during the hydro-blasting process (Dunn, et al., 2011).

The incidences of liner corrosion are believed to be related to the presence of foreign organic material such as wood or felt, and these materials changed the local chemical composition (Dunn, et al., 2011; SNL, 2011). The liner is not expected to develop a through-wall corrosion area when in direct contact with concrete porewater, because the corrosion rate of carbon steel in basic concrete porewater saturated with oxygen is less than $1 \mu\text{m/yr}$ [0.04 mil/yr]. Dunn, et al. (2011) surmised that the foreign objects may retain moisture and promote crevice corrosion by decomposing to produce acidic conditions, which could accelerate corrosion of the carbon steel containment liner.

Every case of through-wall corrosion of the containment liner was detected years after initial plant operation (Dunn, et al., 2011). Dunn, et al. (2011) estimated that corrosion rate at the through-wall corrosion site ranged from 0.3 to 0.5 mm/yr [12 to 20 mil/yr] based on the age of the power plants. This corrosion rate is a few hundred times higher than the corrosion rate of carbon steel in concrete porewater saturated with oxygen, but consistent with corrosion rates in slightly acidic water (Uhlig, 1971). This supports the argument that through-wall corrosion is initiated by foreign organic materials that decompose and produce local acidic conditions. These acidic conditions likely accelerated degradation of the carbon steel containment liner causing through-wall corrosion.

1.2 Inspection Requirements

Because containment liners are credited with acting as leak-tight barriers during an accident condition, they are inspected to ensure they maintain their design bases. The Code of Federal Regulations, Title 10, *Energy*, Part 50, "Domestic Licensing of Production and Utilization Facilities" (10 CFR 50) defines inspection requirements for containment liners, which are mainly inspected following ASME Boiler and Pressure Vessel (B&PV) Code (ASME, 2008) requirements and containment leak rate testing (10 CFR 50.55a and 10 CFR Part 50, Appendix J).

Inspection requirements for metallic liners are detailed in the ASME B&PV Code, Section XI, *Rules for Inservice Inspection of Nuclear Power Plant Components*; Subsection IWE, *Requirements for Class MC and Metallic Liners of Class CC components of Light Water Cooled Plants* (ASME, 2008). The inspection requirements rely mainly on visual examination. These inspections can be performed either directly or remotely, by line of sight from available viewing angles, and with illumination sufficient to detect evidence of degradation. One hundred percent of the surface must be inspected during a 10-year inspection period, which includes inspection subintervals at 3, 7, and 10 years.

In addition to visual inspections, containment leak rate tests are conducted to determine the existence of anomalous leakage from containment. 10 CFR 50 Appendix J provides regulatory guidance for primary reactor containment leakage testing for light water reactors. The containment leak rate test must be conducted periodically to characterize the leak integrity of

the primary reactor containment and the systems and components that penetrate the containment. Three types of leak rate tests are described in 10 CFR Part 50 Appendix J: the Type A test measures the overall integrated leakage rate for a primary containment, while the Types B and C leak rate tests are local leak rate tests used to measure local leakage across each pressure-containing or leakage-limiting boundary.

1.3 Expert Panel Summary

In 2010, The U.S. Nuclear Regulatory Commission (NRC) convened an expert panel to evaluate the incidents of through-wall containment liner corrosion and identify possible causes and contributing factors (SNL, 2011). The panel concluded that degradation was associated with foreign material embedded in the concrete contacting the containment steel liner. The panel surmised that foreign material, such as wood, could lower the porewater pH and locally depassivate the carbon steel, creating an anodic reaction site on the liner. The corresponding cathodic reaction, which involves oxygen reduction, could then be supported by the large area of the liner away from the anodic site, as well as any rebar. This corrosion process, with a large separation between the anode and cathode, is known as macrocell corrosion. The panel report included simplified calculations, using the macrocell corrosion concept, and concluded that macrocell corrosion could very well explain the observed through-wall liner corrosion in domestic power plants. The panel also concluded that other corrosion mechanisms, such as chloride ingress and carbonation, are unlikely given that these processes are controlled by diffusive transport of chemicals and the thick concrete wall limits diffusion.

The expert panel concluded that the current state of nondestructive evaluation is not capable of effectively detecting liner corrosion initiated at the liner outer surface. The panel did not consider mitigation methods, such as cathodic protection, to be practical for preventing liner corrosion. Therefore, visual inspection remains the only practical tool available to detect liner corrosion. As such, corrosion initiated at the liner outer surface can only be discovered when the liner corrosion damage is 100 percent through-wall. Visual inspections will not identify partial corrosion damage.

In this report, a more detailed macrocell corrosion model is developed to (i) evaluate the panel conclusion that the observed through-wall corrosion can be explained on the basis of macrocell corrosion; (ii) estimate damage areas to input into leak rate computations; (iii) investigate the dependence of damage areas on features of the system, such as oxygen diffusivity, concrete ionic resistivity, and rebar placement; and (iv) compute potential leak rates as a function of damage area.

1.4 Objectives

The project consists of two parts: corrosion modeling and leak rate modeling.

The objectives of the corrosion model are to

- Investigate the panel conclusion that observed through-wall corrosion initiated at the external liner surface can be explained as a macrocell-accelerated corrosion process
- Estimate the extent of expected corrosion damage on the liner and associated corrosion rates

- Evaluate factors controlling the corrosion process

The objectives of the leak rate model are to

- Investigate the extent to which liner corrosion damage compromises containment in case of a loss-of-coolant accident (LOCA)
- Estimate leak rates from the containment building in case of liner through-wall corrosion
- Evaluate factors that control leak rates from the containment building

The results of this study are intended to help NRC staff to assess the potential significance of containment liner corrosion and to support regulatory decisions related to this issue.

1.5 Report Organization

The corrosion model is described in Chapter 2. It includes the problem statement, modeling approach, results, and synthesis. Chapter 2 concludes with estimates of corrosion damage areas as input to the leak rate model. Chapter 3 describes the leak rate model and sensitivity analyses. The thermodynamic model and gas transport model are described, as well as results using example LOCA pressure and temperature transients. Chapter 4 is a summary of conclusions. References are included in Chapter 5. The Appendix details alternative approaches to solve mass and charge balance equations of the corrosion model.

2 CORROSION MODEL

The sections in this chapter describe the approach to estimate the extent of liner corrosion damage, with corrosion initiated at the outer liner surface by a piece of foreign wood material. According to the expert panel (SNL, 2011), the operating mode of corrosion is macrocell corrosion. Under macrocell corrosion, the net anode and cathode regions are strongly differentiated, separated by a large distance, with a separation that arises from differing environments around the metal in the liner-rebar-concrete system. The approach to estimate the extent of damage, summarized in Section 2.1, relies on a macrocell corrosion model to compute the net ionic current in the system as a function of the concrete ionic resistivity, and an electrochemical and thermodynamic model to compute the liner current density and corrosion rate as a function of pH. The liner damage area is estimated as the ratio of the macrocell net current and the current density at the anode.

2.1 Approach

A macrocell corrosion model was developed using a finite-element-based computational software. In the range of the concrete ionic resistivity relevant to nuclear power plants ($\rho \sim 10 \text{ k}\Omega\text{-cm}$), it is concluded (in Section 2.5) that the net cathodic current (that balances the anodic current arising from corrosion) can be estimated as

$$I = c r \kappa \Delta E \quad [2-1]$$

where c is a constant approximately equal to 4, r is the anode radius, $\kappa=1/\rho$ is the ionic conductivity, and ΔE is the driving potential. The driving potential, ΔE , is defined as the difference between the far cathode potential and the anode potential.

Anodic current densities (which are proportional to corrosion rates) were computed using the OLIAnalyzer Studio[®] Version 9.0 software (OLISystems, Inc., 2013). This software is a thermodynamic–kinetic code that has been validated over a range of chemical compositions, concentrations, temperatures, and pressures (Anderko, et al., 2001; Anderko, 2010). The code computes the aqueous speciation in the investigated system using a thermodynamic model of electrolyte systems that combines information on the standard-state properties of all species of interest with an excess Gibbs energy formulation to account for solution non-ideal behavior. The code also has an electrochemical model that takes into account reactions on the surface of the metal and transport processes for the species that participate in the reactions and includes passivation phenomena. The electrochemical model also combines the partial processes to compute corrosion rates in the framework of the mixed potential theory (Anderko, et al., 2001).

Representative concrete porewater compositions, with a pH controlled by acetic acid, an organic acid present in wood, and minimal oxygen concentration were considered to compute corrosion rates at 60 °C [140 °F] as a function of the anode potential. If i_{max} represents the maximum current density for the anode, for a fixed electrolyte composition and temperature, the following expression was used to determine the net current in the macrocell

$$I = c \kappa r \Delta E = i_{max} \pi r^2 \quad [2-2]$$

equivalently

$$r = \frac{c \kappa \Delta E}{\pi i_{max}} \quad [2-3]$$

from which the anode area is computed as $A = \pi r^2$.

A finite-element differential equation solver software was used to construct a macrocell corrosion model that accounts for oxygen diffusion, oxygen reduction at the rebar steel and passive liner, and ionic current from the anode to the cathode. Parametric studies were performed to analyze the change in net current as functions of the anode potential, rebar separation, oxygen diffusion coefficient, concrete ionic resistivity, and anode size, and it is concluded that Eq. [2-1] holds valid for the cases of interest (see Section 2.5).

Equation [2-3] is used as a synthesis equation to estimate ranges of damage areas. A Monte Carlo approach is adopted that accounts for reasonable ranges of the concrete ionic resistivity, cathode potential, anode potential, and solution pH to estimate the range of damage area by corrosion. The synthesized model to compute the liner damage by corrosion was coupled to the leak rate model described in Chapter 3.

2.2 Macrocell Corrosion Background

Macrocell corrosion differs from other forms of corrosion (e.g., pitting and crevice corrosion) in that the dimensions separating the anode and cathode are large, spanning from millimeters up to meters (Gulikers, 2005; Kranc and Sagüés, 1994). The separation arises due to different chemical conditions around the anode and the cathode. A schematic of the macrocell corrosion process for the liner-rebar-concrete system is presented in Figure 2-1.

Figure 2-1 shows the carbon steel liner and reinforced concrete in close contact. The structural rebars are in electrical contact with the liner (contact not represented in Figure 2-1). As the expert panel argued (SNL, 2011), degraded wood can lower the pH of the porewater and activate the steel underneath. This active liner region is the anode. The predominant chemical

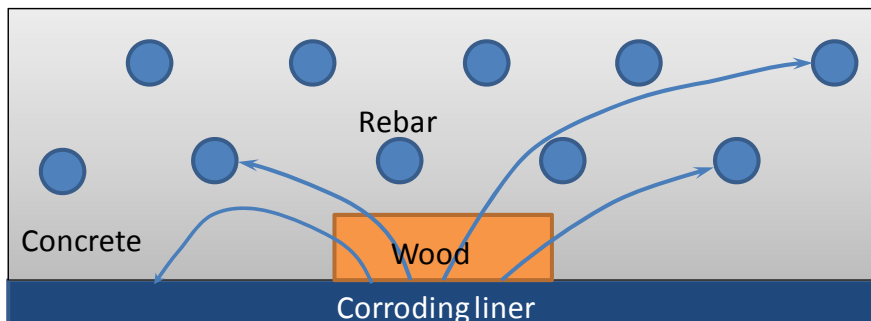


Figure 2-1. Schematic Representation (Not To Scale) of the Macrocell Corrosion Process for the Liner and Concrete Containment System. The Blue Lines Represent Ionic Current Lines. The Rebars and Section of the Liner, Where Current Lines Enter, Act as Cathode. The Liner and the Rebars Are in Electrical Contact.

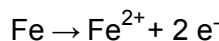
reaction that occurs in the active region is iron dissolution, which is a charge transfer reaction that generates electrons that are transported through the steel (as previously stated, the liner and the rebar are most likely in electrical contact). These electrons are consumed by oxygen reduction reactions that could occur either at the passive surface of the rebars or at the passive liner surface (at a distance from the active region), or both. The blue arrows in Figure 2-1 represent the ionic current directions in the macrocell.

Oxygen reduction reaction is more intense at rebars closer to the atmosphere (top rebars in Figure 2-1) than at the passive liner because oxygen must diffuse a longer distance to reach the passive liner. In addition, oxygen is consumed by the oxygen reduction reaction at the rebars; thus, the oxygen concentration in the concrete decreases in the direction from the atmosphere to the liner (down direction in Figure 2-1). The anode–cathode separation causes the formation of an electric field in the concrete, which supports the establishment of ionic currents. The concrete ionic resistivity is a measure of how difficult it is to establish those ionic currents. For example, if the resistivity is low (i.e., high ionic conductivity), the magnitude of the ionic currents is higher. If the ionic resistivity is high, the magnitude of the ionic current is lower, making it difficult to sustain the corrosion process. The oxygen reduction reaction and iron dissolution reaction also depend on the electrode potential. The electrode potential at the anode is lower (i.e., more electronegative) than the potential at the cathode. The difference between anode and cathode potentials is a measure of the overall potential gradient, or electric field, in the macrocell. The rate of the oxygen reduction reaction increases with decreasing values of the electrode potential. Thus, the rate of oxygen reduction reaction tends to be higher at the rebars and passive liner region near the anode; however, oxygen diffusion transport limitations also compete for the establishment of balanced reaction rates.

In summary, there are two driving forces that control the rate of oxygen reduction reaction (i) the gradient in electrode potential and (ii) rate of oxygen supplied by diffusion. Also, there are two factors that control the establishment of ionic current (i) an electric field (with a magnitude depending on the potential difference between anode and cathode) and (ii) the concrete ionic resistivity. An electrochemical cell is established (promoting corrosion) when the ionic current is balanced by the oxygen reduction reaction. Interplay of the driving forces and the factors controlling the ionic current determine the extent of corrosion at the anode. For example, if the concrete ionic resistivity is high, the current generated at the anode would be low for a given gradient in electric potential. A low current at the anode indicates either a low corrosion rate or a small anode size. If the resistivity is too large, macrocell corrosion is unlikely. On the other hand, if oxygen is not readily available, then the ionic current must be also low, also indicating a low corrosion rate or a small anode size.

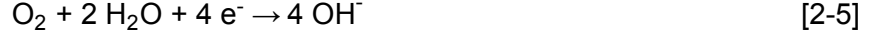
2.3 Model Description

The macrocell corrosion process is modeled as a charge and mass balance system under steady-state. Thus, being steady-state, propagation of the corrosion damage and the corrosion front are not described by the model. The liner and the rebars are considered in electrical contact; therefore, the liner–rebar is a unit where electrons travel freely. The electrical contact between the liner and rebars is established by studs on the liner, which were tied to the concrete containment rebars (e.g., see Figure 5 in Dunn et al., 2011). The anodic or corrosion reaction in the active region of the liner (i.e., the anode) is iron oxidation reaction (Krac and Sagüés, 2001).



[2-4]

The cathodic reaction at the rebars and passive liner (i.e., the cathode) is the oxygen reduction reaction



The macrocell is a current–balance system. The anode is a source of positive ions and electrons as specified in Eq. [2-4]. Electrons flow through the metal, from the anode to the cathode, and are consumed at the cathode by the oxygen reduction reaction, Eq. [2-5]. For the cell circuit to be completed and the electronic charge to be balanced by the ionic charge, an ionic current of the same magnitude as the electronic current develops in the concrete. The driving force for the ionic current through the concrete is the electric field, which has a magnitude related to the difference between the anode and cathode electrode potentials. Neglecting diffusive components contributing to ionic currents, the ionic current, i_b , is computed using Ohm's law

$$i_b = -\kappa \nabla \phi \quad [2-6]$$

where ϕ is the solution potential of the concrete in the unit of volts, κ is the ionic conductivity of concrete in units of $\Omega^{-1}\text{cm}^{-1}$, and i_b is in units of A/cm^2 . The charge conservation equation (no net charge generated or lost in the concrete medium) can be stated as $\nabla \cdot i_b = 0$ or

$$\nabla^2 \phi = 0 \quad [2-7]$$

The symbol ϕ , referred as *solution potential*, differs from the *electrode potential*. The solution potential defines, through its gradient, the electric field that transports ions in the concrete. The electrode potential is the potential measured at the metal with respect to a reference electrode, ideally placed in the electrolyte immediately facing the metal surface. The metallic assembly of liner and rebar is assumed to be interconnected and highly conductive, so its potential is effectively constant and assigned a ground value of zero. Following commonly used conventions (Krank and Sagüés, 2001), the solution potential at positions immediately facing steel surfaces is related to the electrode potential by $\phi = -E$.

Availability of oxygen to the cathode can be computed by estimating the flux of oxygen according to Fick's law

$$J_{O_2} = -D_O \nabla C_{O_2} \quad [2-8]$$

where D_O is the oxygen diffusion coefficient (in units of cm^2/s) and C_{O_2} is the oxygen concentration, chosen here to be expressed as that in the concrete porewater (in units of mol/cm^3). It is noted that alternative ways exist of defining C_{O_2} (Sagüés, et al., 2003; Huet, et al., 2007) and that the corresponding numeric value of D_O must be chosen accordingly. The mass conservation equation under steady state requires that $\nabla \cdot J_{O_2} = 0$ or

$$\nabla^2 C_{O_2} = 0 \quad [2-9]$$

The charge and mass conservation equations, Eqs. [2-7] and [2-9], are coupled only by the boundary conditions at the cathode, which are discussed in the following paragraphs. Once the potential distribution, ϕ , is determined, the net current in the system, I , can be computed, which is related to the corrosion rate and size of the anode.

Boundary Conditions

The chemistry of the porewater is likely to be variable along the anode surface, and, similarly, the solution potential is expected to be variable along the anode surface. To simplify the problem, the anode is approximated as a constant potential boundary. This constant anode potential is an input parameter, which is varied from simulation to simulation. The potential distribution in the concrete domain for each value of the constant anode potential is determined by solving the mass and charge balance differential equations, and the net current in the system is computed as a function of the steady-state electric potential distribution. Because of the assumption of constant potential, the anode is implicitly assumed to exhibit a uniform corrosion rate. However, as previously stated, in reality both the potential and the porewater chemistry are likely to vary along the anode surface. This variability would cause the corrosion rate to also vary along the anode surface, and make the corrosion front become non-uniform. Description of the propagation of a non-uniform corrosion front is a complex problem. In this report it was opted to analyze a simplified system. The adopted simplification (i.e., constant-potential anode) allows for the derivation of trends that are used in the approach to estimate corrosion areas. The dependence of the results on the magnitude of the anode polarization and anode corrosion rate is explored through sensitivity analyses. Section 2.8 provides suggestions to deal with variability (in pH and polarization) on the anode surface.

At the cathode, the current density is related to the solution potential gradient just outside the interface of the metal and concrete according to Ohm's law

$$i_c = \kappa \vec{n} \cdot \nabla \phi \quad [2-10]$$

where i_c denotes the current density at the cathode in units of A/cm^2 , κ is the ionic conductivity of concrete in units of $\Omega^{-1}\text{cm}^{-1}$, and \vec{n} is an outward unit normal vector to the metal surface. The current at the cathode is related to the kinetics of oxygen reduction according to the following equation (Kranc and Sagüés, 1994)

$$i_c = i_{O_2}^o \exp\left(\frac{\phi - \phi_o}{\beta_c}\right) \frac{C_{O_2}}{C_{O_2}^o} - i_{pass} \quad [2-11]$$

where $i_{O_2}^o$ is a constant with units of current density, ϕ_o is an equilibrium potential with units of volts, β_c is a Tafel slope with units of volts, $C_{O_2}^o$ is a reference concentration, and i_{pass} is the iron passive current density. It is considered that steel undergoes passive corrosion, and therefore the oxygen reduction consumes the electrons locally produced by the passive dissolution. Note that Eq. [2-11] includes a term proportional to the oxygen concentration, C_{O_2} , which causes a coupling between oxygen transport by diffusion and ionic transport under an electric field. In addition, the oxygen flux at the metal surface is proportional to the ionic current arriving at the cathode

$$\vec{n} \cdot D_O \nabla C_{O_2} = \frac{i_c}{nF} \quad [2-12]$$

where \vec{n} is the outward unit normal vector to the metal surface, F is the Faraday constant (equal to 96,500 Coul/mol), and $n=4$ is the number of electrons in the cathodic reaction in Eq. [2-5]. Equations [2-11] and [2-12] can be combined as

$$4 F \vec{n} \cdot D_O \nabla C_{O_2} = \overline{i_{O_2}^o} \exp\left(\frac{\phi}{\beta_c}\right) \frac{C_{O_2}}{C_{O_2}^o} - i_{pass} \quad [2-13]$$

which makes more evident the coupling between the solution potential, ϕ , and the oxygen concentration, C_{O_2} . In Eq. [2-13], $\overline{i_{O_2}^o} = i_{O_2}^o \exp\left(-\frac{\phi_o}{\beta_c}\right)$.

At the interface between the concrete and atmosphere, a constant concentration is applied

$$C_{O_2} = C_{O_2}^{atm} \quad [2-14]$$

where, following the choice indicated earlier, $C_{O_2}^{atm}$ is the oxygen concentration in water in equilibrium with oxygen in air at ambient conditions.

2.4 Model Implementation

A differential equation solver, COMSOL Multiphysics (COMSOL, Inc., 2013), was used to solve the coupled system of Eqs. [2-6] to [2-14] for the liner-rebar-concrete system. The following abstractions and simplifications were adopted:

- The anode is a disc, modeled as a constant potential surface.
- The system is axisymmetric.
- The rebar geometry is simplified as a series of concentric rings.
- At a distance from the anode, only the rebars located closer to the atmosphere are explicitly included in the model, as other rebars will minimally contribute to the net current.

An example of the rebar placement and mesh geometry is presented in Figure 2-2. The complete modeled domain has a radius of 8 m [26.2 ft]. This domain is sufficiently large that metal surfaces beyond this radius do not contribute to the net cathodic current balancing the current originating at the anode. The liner is located at the bottom of the domain, and it is included in the model through the boundary conditions. The atmosphere is at the top of the domain. Figure 2-2(b) is an expanded view of the mesh. The mesh in the anode is dense, because most of the variability in the solution potential occurs near the anode.

The abstraction of rebars as rings is intended to represent the fact that cathodic sites are available at discrete sites. The rebar geometry is not important to determine the solution potential distribution. It is more important to properly capture the availability of carbon steel surface per unit of concrete volume. A surface factor was used to adjust (increase or decrease) the surface area of the rebar in the model. The adjustment factor was used in the boundary conditions at the rebars. This adjustment factor does not significantly change the net current in the range of concrete ionic resistivity of interest, as discussed next.

A couple of approaches were explored to define and solve the differential equations. The methods, polarization curves, and model parameters are detailed in the Appendix. The need to explore alternative methods arose to address convergence issues in the oxygen concentration

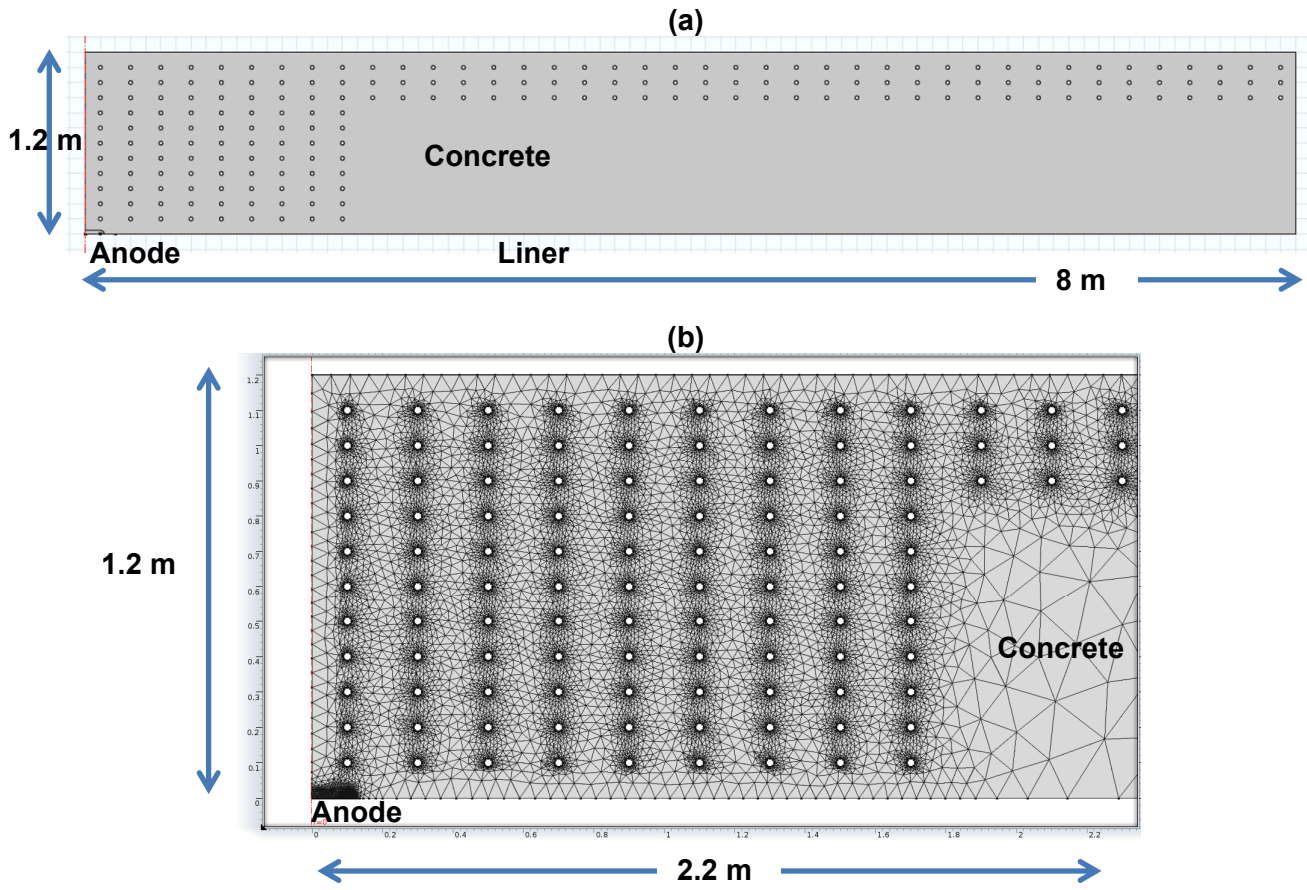


Figure 2-2. Example of Finite Element Mesh to Numerically Solve the Differential Equations. (b) Is an Enlarged Section of (a).

initially experienced. Method 1 in the Appendix implemented approximations and alternative boundary conditions to solve for the electric potential distribution. The current density at cathode sites is defined, in Method 1, using an equation Warkus, et al. (2006) proposed, which includes terms for oxygen reduction, iron passive current density, and oxygen transport limited current density. In Method 1, Eq. [2-13] is not used to couple oxygen concentration to ionic transport. Instead, an approximated linear gradient equation is used to compute a limiting value of the current density at the cathode as a function of the oxygen penetration depth and the oxygen porewater concentration at the concrete and atmosphere interface. Convergence problems were successfully addressed using Method 2 in the Appendix. The set of Eqs. [2-6] to [2-14] are solved in Method 2, with parameters of the oxygen reduction rate as a function of the solution potential computed using the OLIAnalyzer Studio software (OLISystems, Inc., 2013). Both methods produced nearly identical results (net current versus driving potential), despite using different parameters to define the oxygen reduction rate as a function of the solution potential and oxygen concentration (e.g., see Section 2.5). Therefore, it is concluded that uncertainty in the rate of oxygen reduction as a function of the solution potential does not affect the results and conclusions attained in this report. Figure 2-3 is an example of the solution potential distribution, ϕ , and lines of current.

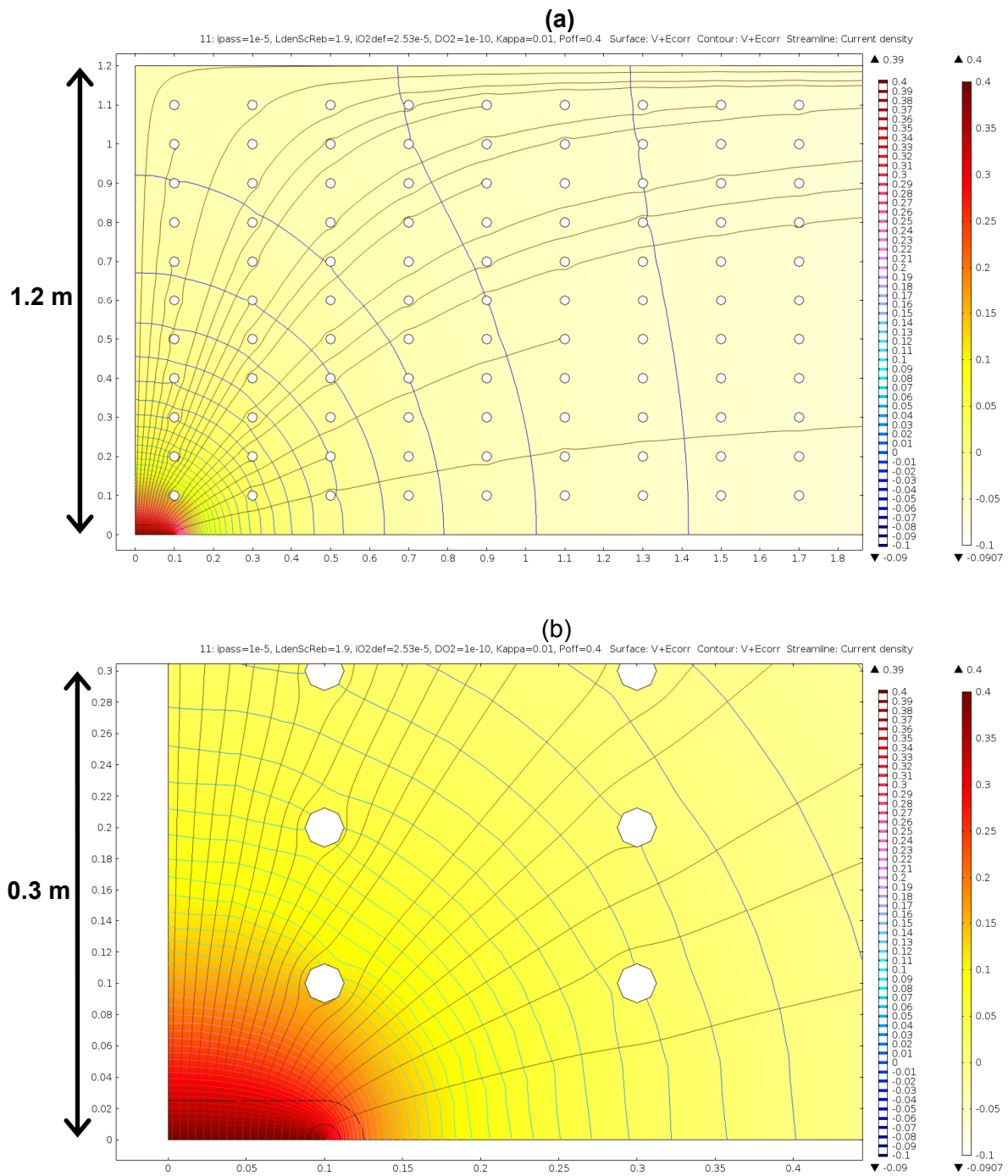


Figure 2-3. Example Distribution of the Solution Potential (Contours Forming Approximate Circles) and Current Lines (Lines Emanating From the Anode). The Anode Electrode Potential is $E=-400 \text{ mV}_{\text{SHE}}$ [i.e., $\phi(\text{anode})=400 \text{ mV}$]. The Scale in the Figure Corresponds to the Solution Potential, ϕ . (a) and (b) Show the Same Solution Potential Distribution at a Large and a Small Scale, Respectively. Oxygen Diffusion Coefficient, $D_o = 10^{-6} \text{ cm}^2/\text{s}$.

As previously discussed, the electrode (i.e., metal) potential is defined as $E = -\phi$. For example, a potential of $\phi = 100$ mV corresponds to an electrode potential of $E = -100$ mV measured versus standard hydrogen electrode (SHE), denoted as $E = -100$ mV_{SHE}. Potentials are specified in volts, but the reader should keep in mind the conversion between solution potential and electrode potential, and that electrode potentials are measured versus SHE.

Figure 2-3 shows isopotential lines and current lines (perpendicular to the isopotential lines). A number of current lines are shown to end at rebars. The distal potential (potential far from the anode) is approximately $\phi = -100$ mV, corresponding to an electrode potential of $E = 100$ mV_{SHE}, which is a reasonable value observed in slightly deaerated concrete (Bertolini, et al., 2004). In the expanded view in Figure 2-3(b), current lines diverge from the anode in a configuration very similar to current lines that would be established if the cathode was an infinite plane located far away. As discussed in Section 2.6, it is argued that the results are consistent with the limiting case of a disc anode with a large counter electrode located at infinity.

Figure 2-4 shows the oxygen distribution and the effect of the anode potential on the oxygen distribution. In this example (oxygen diffusion coefficient $D_o = 10^{-6}$ cm²/s), the oxygen concentration is relatively abundant in the concrete near the atmosphere and the oxygen is depleted near the anode. Figure 2-4(a) differs from (b) in the anode potential. As the anode potential is decreased in Figure 2-4(b), the rate of oxygen reduction is decreased, and this explains why the oxygen front is deeper in Figure 2-4(b).

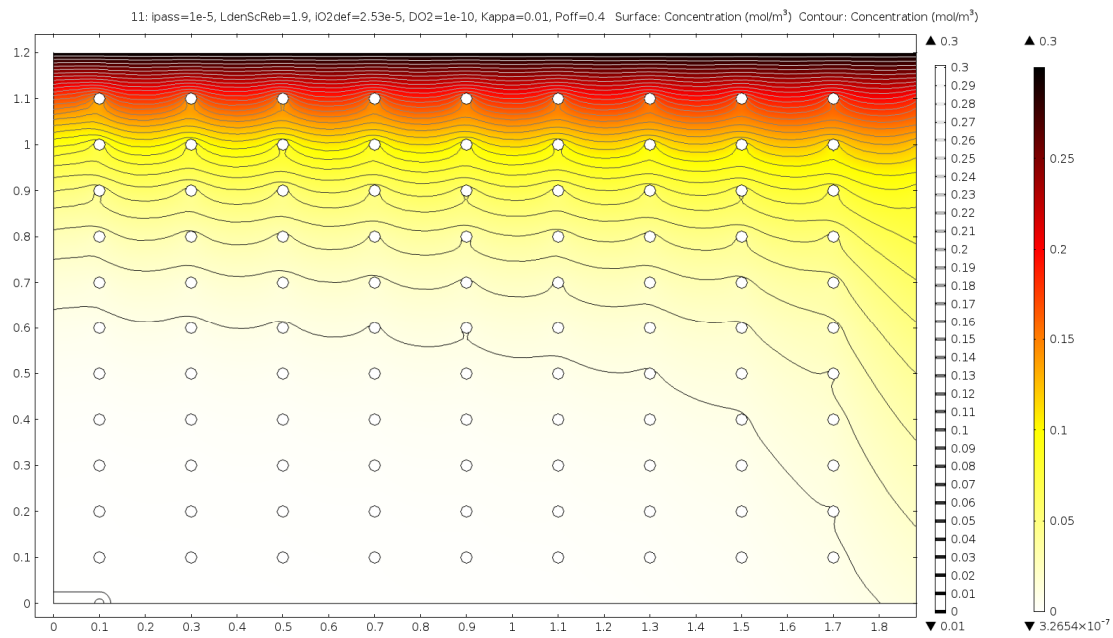
Figure 2-5 shows another example of potential and oxygen distribution obtained with a high value of the oxygen diffusion coefficient ($D_o = 10^{-5}$ cm²/s). The larger effective diffusion coefficient considered in the computations in Figure 2-5 caused oxygen to penetrate deeper, compared to Figure 2-4(b). Oxygen is abundant throughout the concrete, and only scarce near the anode in this simulation.

Simulations were performed varying model parameters to investigate their effect on estimates of the net current. The potential and oxygen concentration distributions are similar to the examples in Figure 2-3 through 2-5. The results of the parametric studies are summarized in the next section.

2.5 Sensitivity Analysis on the Net Current

Numerous simulations were performed varying the kinetic parameters (i_{pass} and $\overline{i_{O_2}^G}$), the oxygen diffusion coefficient, and the rebar surface factor (varying one parameter at a time) to investigate the effect of these parameters on estimates of the net current. The parametric studies were conducted to evaluate uncertainty in the concrete ionic resistivity, the rebar density, kinetic and diffusion parameters, concrete heterogeneity, and variations due to the elapsing of time (e.g., there are temperature variations due to the power plant cycles; the concrete changes due to drying and slow formation of secondary compounds). Table 2-1 summarizes discrete values of parameters in the sensitivity studies. It should be noted that parameters were selected over broad ranges, which do not necessarily represent actual operating conditions for a nuclear power plant containment setting. The objective of the parametric study was only to identify general mathematical trends that could be used in the estimates of the corrosion area.

(a) $\phi(\text{anode}) = 400 \text{ mV}$



(b) $\phi(\text{anode}) = 100 \text{ mV}$

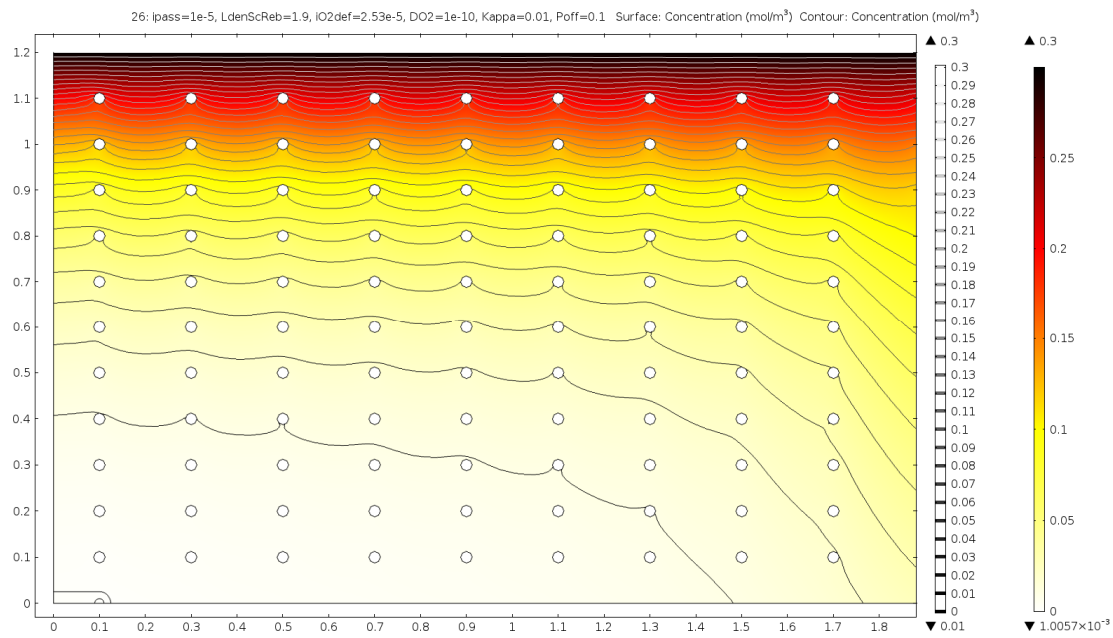
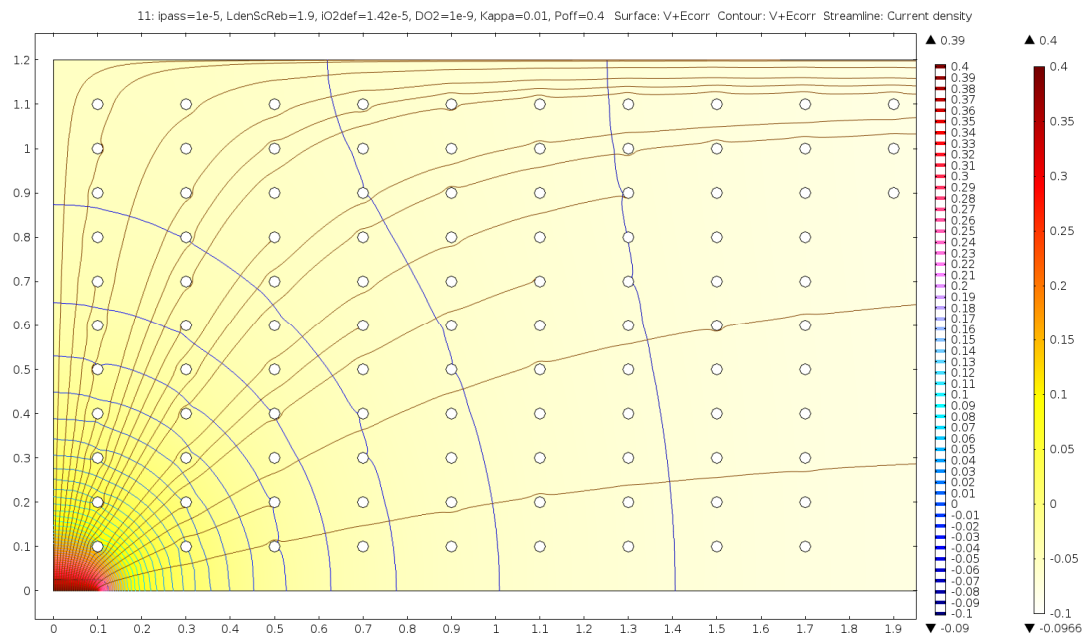


Figure 2-4. Effect of the Anode Potential on the Oxygen Distribution. (a) Solution Potential Near the Anode = 400 mV and (b) Solution Potential Near the Anode = 100 mV. Oxygen Diffusion Coefficient, $D_o = 10^{-6} \text{ cm}^2/\text{s}$.

(a)



(b)

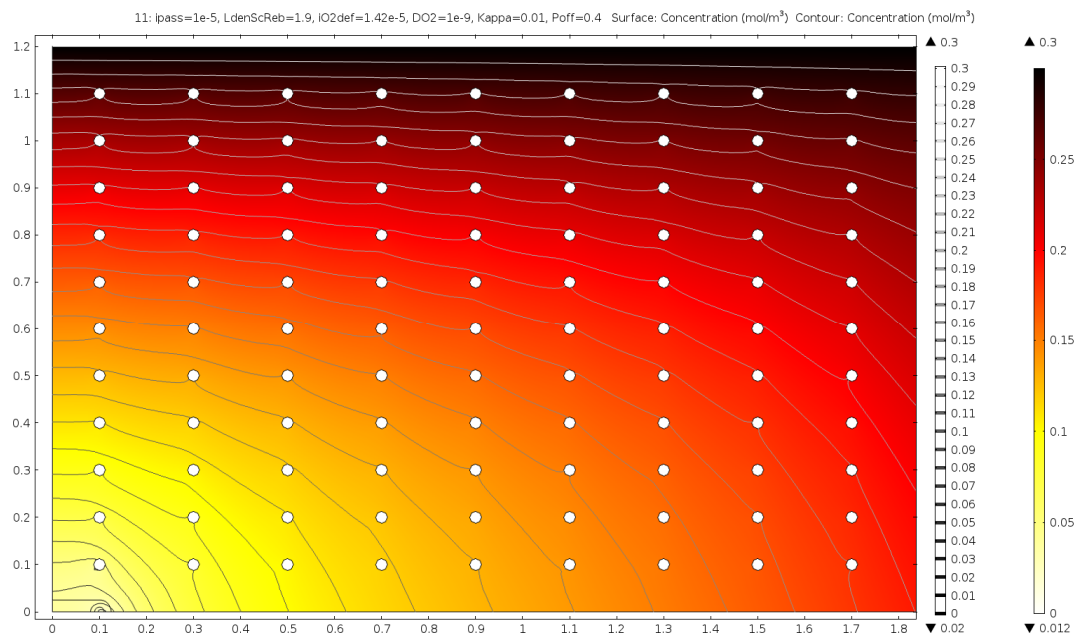


Figure 2-5. Example of Potential (a) and Oxygen Distribution (b) Obtained With a High Value of the Oxygen Diffusion Coefficient ($D_O = 10^{-5} \text{ cm}^2/\text{s}$). The Anode Potential is 400 mV.

Table 2-1. Parameter Values Considered in the Parametric Studies

Parameter	Values
ρ	1, 10, 100, 1000 k Ω -cm
D_o	$10^{-7}, 10^{-6}, 10^{-5}, 10^{-4}$ cm 2 /s
i_{pass}	0.001, 0.01, 0.1 μ A/cm 2
$i_{O_2}^o$	0.25, 2.5, 25 μ A/cm 2
Rebar factor (rebar volume fraction)	1.5, 4.5, 15 percent
Anode potential	-0.6 to 0.3 V _{SHE}
Anode radius	1, 5, 10, 20 cm

The comparison curve in the parametric studies was the net current, I , as a function of the driving potential, ΔE . The driving potential is defined as the difference between the anode potential and the cathode potential at a distant location from the anode. The distal potential was computed as an average of the electrode potential at a radial distance of 8 m [26.2 ft]. This distal potential is interpreted as an average corrosion potential or equilibrium potential, in the absence of localized corrosion. The word *average* is used to recognize the fact that the corrosion potential is a function of the oxygen concentration and that the oxygen concentration varies with depth along the concrete. We explored alternative approaches to define the driving potential, but the results were practically the same. For example, in Method 1 detailed in the Appendix, the corrosion potential at the rebar closest to the atmosphere is provided as a model input, and the driving potential is defined as the difference between the anode potential and the input corrosion potential. The net ionic current can be computed in several manners. For example, it can be computed as the total current emanating from the anode [e.g., see Figure 2-3(b)]. Also, it can be computed by integrating all current ending at the cathode surfaces [e.g., Figure 2-3(a) shows a number of current lines with end points at rebars]. Both approaches were used, which provided slightly different results, typically varying less than 8 percent. The net current reported in this section was computed by integrating the ionic current emanating from the anode.

From the parametric studies it is concluded that the concrete ionic resistivity is the most important parameter determining the net ionic current. For example, Figure 2-6 shows the net current as function of the driving potential and the concrete ionic resistivity, considering an electrode 10 cm [3.94 in] in radius and the standard method, (Appendix, Method 2). The scatter in Figure 2-6 is the result of the variation of the kinetic parameters, the oxygen diffusion coefficient, and the rebar coverage factor. In Figure 2-7, the alternative Appendix Method 1 was used. In this case the scatter is the result of variation in the oxygen diffusion coefficient. In both methods, order of magnitude variation in the resistivity ρ causes order of magnitude variation in the net current, evidenced by the very different vertical axis scales. The other parameters cause a smaller variation in the net current. The red line, in all cases, is computed as

$$I = c \frac{r}{\rho} \Delta E \quad [2-15]$$

where $c=3.5$, r is the anode radius, ρ is the concrete ionic resistivity, and ΔE is the driving potential. Figure 2-8 shows the variation of the net current as a function of the model parameters using the standard method. Only the case $\rho = 100$ k Ω -cm is shown in Figure 2-8, but the other resistivity cases exhibited similar trends. The linear trend in Eq. [2-15] is an ohmic behavior that arises in the limit when the anode and cathode are separated by a long distance, as explained in Section 2.6.

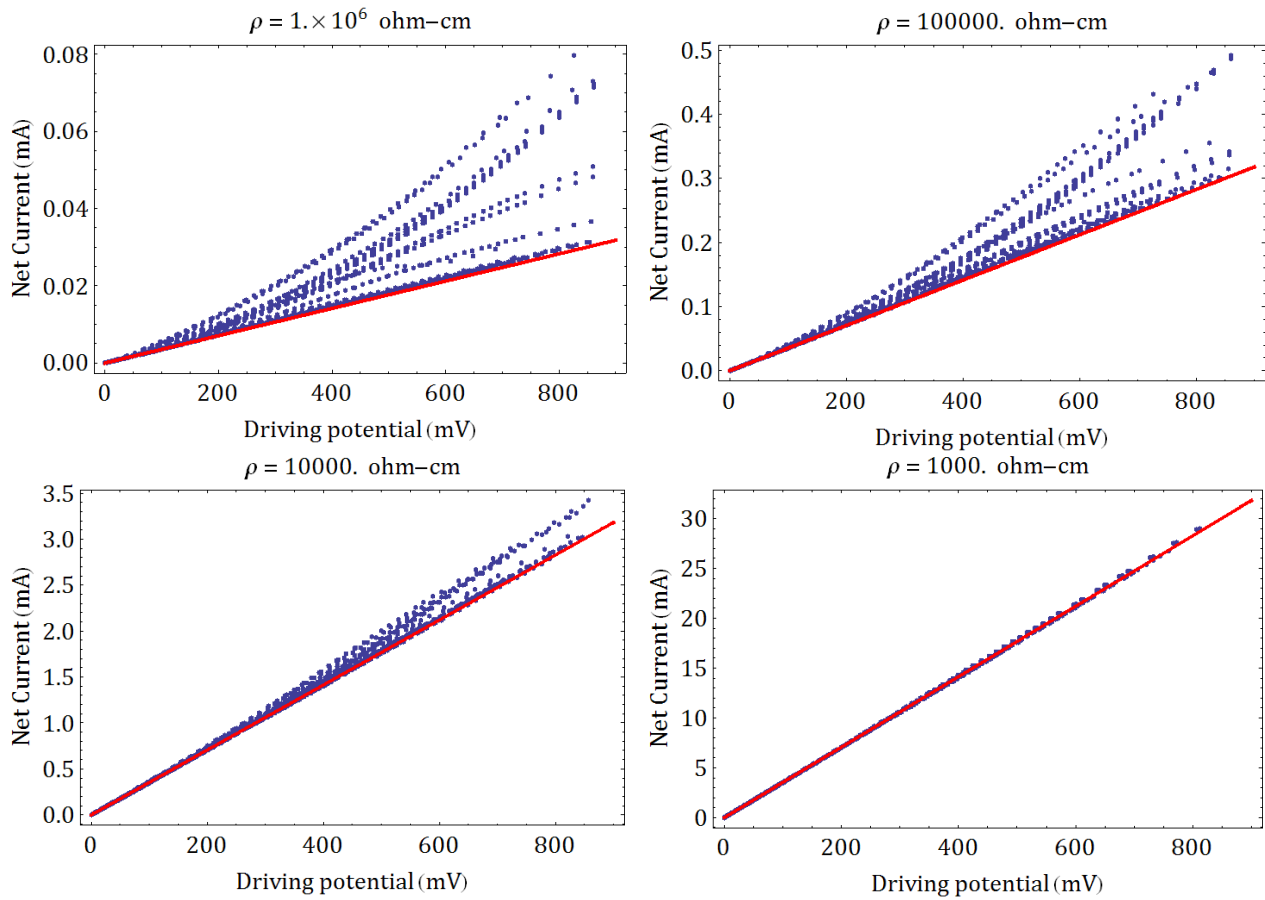


Figure 2-6. Net Ionic Current Versus Driving Potential. The Anode Was a Disc of Radius 10 cm [3.94 in]. Data Derived Using the Method 2 in the Appendix (Referred to as the Standard Method). The Scatter Is Due to Variation in Kinetic Parameters, Oxygen Diffusion, and Rebar Coverage Factor in the Simulations.

Figure 2-8(a) shows the variation of the net current as a function of the oxygen diffusion coefficient. With increasing diffusivity, the net current increases. In Figure 2-8(b), the net current tends to decrease with increasing value of the passive current density, i_{pass} . The net current decreases because the net current is an excess current: net current = oxygen reduction current–passive dissolution current. Therefore, if the passive current density increases, the excess current decreases. The variation in the parameter $\overline{i_{O_2}^0}$ did not result in any systematic trend in the net current in Figure 2-8(c). Also, there is no clear trend in Figure 2-8(d) arising from the variation of the net current as a function of the rebar factor. The rebar factor can be interpreted as a volume fraction in percent units. For example, a factor of 1.5 means that the volume of the rebar divided by the concrete volume is 1.5 percent. Competing factors make the trend not unidirectional. For example, increasing the volume fraction increases the availability of metal surface for oxygen reduction, which increases the net current; however, because rebar undergoes passive corrosion, as noted in Figure 2-8(b), increasing the extent of passive current (through an increase in the rebar volume fraction) causes a decrease in the net current.

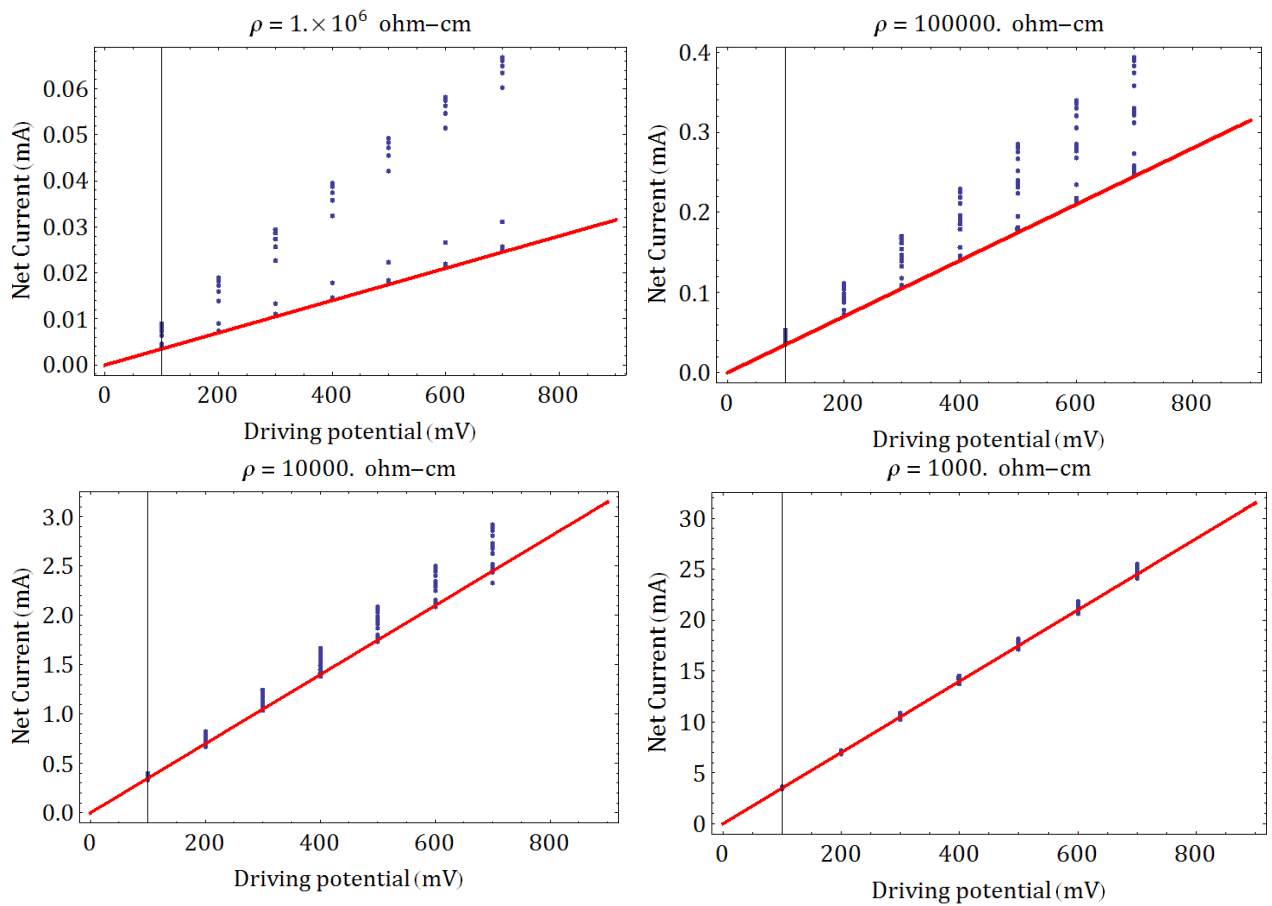


Figure 2-7. Net Ionic Current Versus Driving Potential. The Anode Was a Disc of Radius 10 cm [3.94 in]. Data Derived Using the Alternative Method 1 in the Appendix. The Scatter Is Due to Different Selection of Oxygen Diffusion Coefficients in the Simulations.

Additional analyses varying the anode radius were performed to identify the effect of the anode area on the net current. A limiting curve (e.g., red line in Figure 2-6) of the form $I = \bar{c} \Delta E$, where \bar{c} is inversely proportional to the resistivity, ρ , and approximately linearly proportional to the anode radius, was also derived with other values of the anode radius. This equation is consistent with the theoretical equation for a disc electrode with an infinite counter electrode located at a far distance (see Section 2.6).

The range of concrete ionic resistance, suggested by the expert panel report (SNL, 2011), is from 1 k Ω -cm to 100 k Ω -cm. The panel inferred that the water to cement ratio (w/c) of the concrete used in the construction of the containment structure was likely to be 0.5 or greater (SNL, 2011). Concrete with high w/c and low water saturation can have a resistivity as high as 100 k Ω -cm, with resistivity decreasing with increasing water saturation (Ozbolt, et al., 2011). Given the thickness of the concrete wall {120 cm [3.94 ft]}, it is expected that the concrete would keep most of its original high moisture, and in that case, resistivity values around 10 k Ω -cm are likely (Neville, 1996).

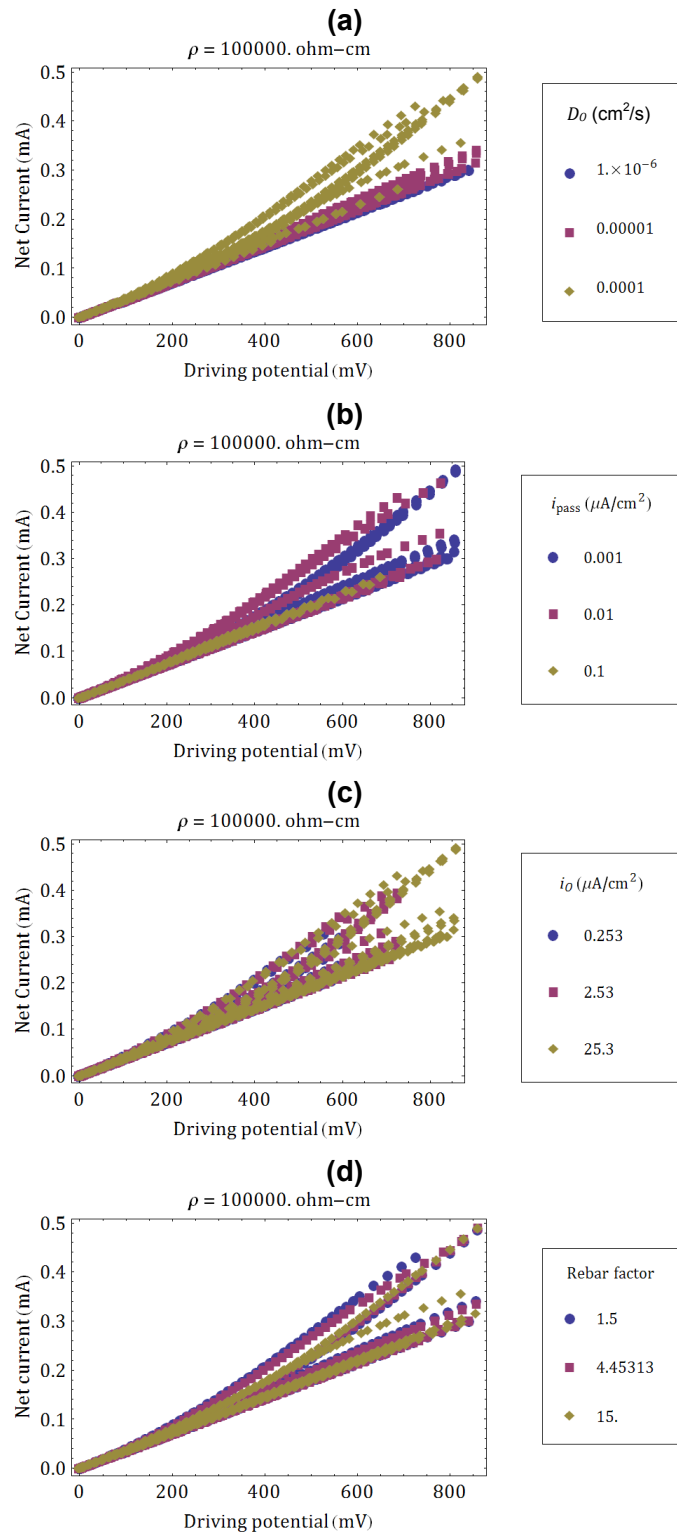


Figure 2-8. Variation of the Net Current As Function of the Driving Potential and Model Parameters. The Concrete Ionic Resistivity Was 100 k Ω -cm and the Anode Was a Disc of Radius 10 cm [3.94 in].

Note that the effect of uncertainty or variability in kinetic parameters and oxygen diffusion coefficient is minor in Figure 2-6 when the resistivity is on the order of 10 k Ω -cm or smaller. It is only in cases of large resistivity ($\rho > 100$ k Ω -cm) where variation, for example, in the diffusion coefficient has a significant effect on the net current. The net current can increase if oxygen is readily available and diffuses fast.

2.6 Limiting Case: Disc Electrode with an Infinite Counter Electrode at a Far Distance

It is concluded from the analysis in Section 2.5 that the net cathodic current that balances the anodic current arising from liner corrosion is function of the following factors: (i) concrete ionic conductivity, (ii) electrode potential difference between anode and cathode, and (iii) size of the anode. The precise functionality between the net cathodic current and the factors is given by

$$I = c r \kappa \Delta E \quad [2-16]$$

where c is a constant approximately equal to 4, r is the anode radius, κ is the ionic conductivity, and ΔE is the driving potential. Equation [2-16] matches the asymptotic solution for a disk electrode system described by Newman (1966). Newman (1966) analyzed a system where a disk electrode is embedded in an insulating plane as shown in Figure 2-9(a). The disk electrode is equivalent to the anode in the macrocell corrosion model for the liner-rebar system, depicted in Figure 2-9(b). In the disk electrode system, the counter electrode is located far away (infinite

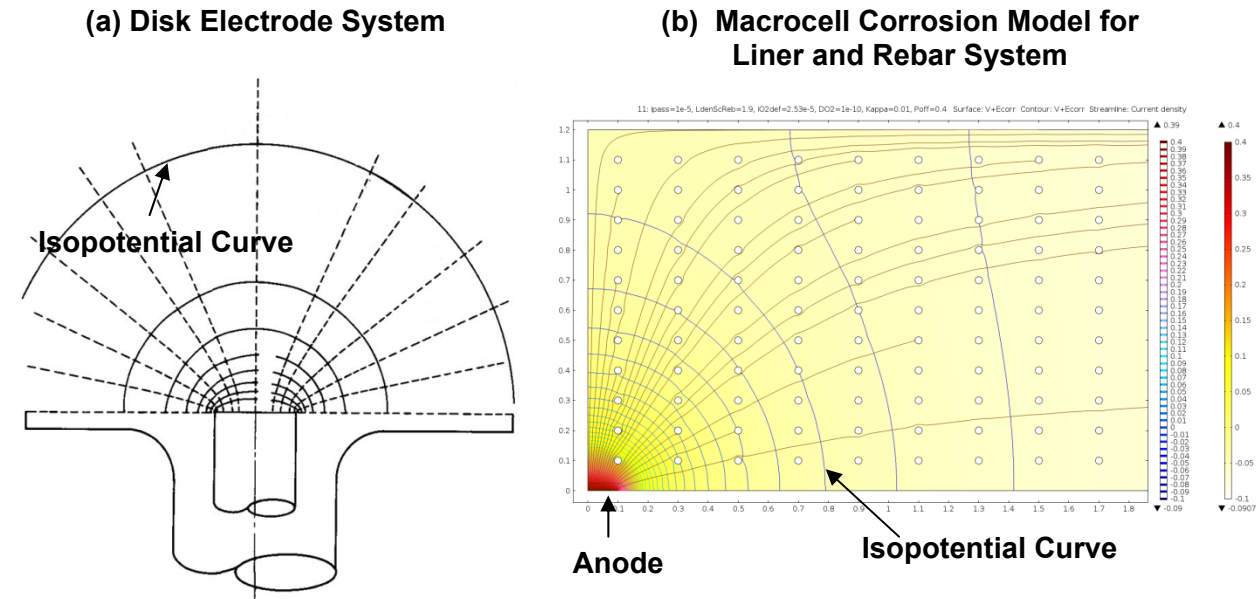


Figure 2-9. Comparison of the Disk Electrode System to the Macrocell Corrosion Model of Liner and Rebar System (Newman, 1966)
[Reproduced With Permission From The Electrochemical Society]

distance from the anode). Newman only considered ohmic resistance to the charge flow through electrolyte and obtained Eq. [2-16] as expression for the current between the disk electrode and the counter electrode, with $c=4$. Newman disregarded kinetic effects at the disk and counter electrodes under the assumption that resistance to the charge flow is controlled by transport through the electrolyte. Newman also assumed that the disk electrode is maintained at a constant potential.

Newman's disk electrode system resembles the macrocell corrosion model for the liner-rebar system for the following reasons. The isopotential lines are approximately semi-circular around the disk electrode and are perpendicular to the insulating plane in Figure 2-9(a). Similar isopotential lines are noted in the macrocell corrosion model in Figure 2-9(b) near the anode. This indicates that the liner surface adjacent to the anode does not contribute to the net current and, hence, is equivalent to the insulating plane in the disk electrode system. The counter electrode in Newman's disk electrode system is located far away from the disk. The rebars that contribute to the net current in the macrocell corrosion model are also far from the anode. In fact, most of the net cathodic current is associated with rebars closer to the atmosphere. This can be observed from the oxygen concentration distributions depicted in Figure 2-4. In those simulations, little or no oxygen is available to rebars close to the anode. Thus, rebars with excess cathodic current to sustain the galvanic cell are located far from the anode.

In the disk electrode system, Newman (1966) assumed that the charge transfer resistance at the disk and counter electrode is equal to zero. Newman concluded that the electrolyte resistance, R , for the disk electrode system is calculated with the following equation

$$R = \frac{\rho}{4r} \quad [2-17]$$

which yields a value $c=4$ for the constant c in Eq. [2-16]. Consistent with this result, the COMSOL simulations in Section 2.5 indicate a value for c close to 4.

To compare to Newman's assumption of negligible charge transfer resistance, the charge transfer resistance in the macrocell corrosion model was estimated using the cathode electrode kinetics expressions in Method 1 from the Appendix. Additional details for estimating the charge transfer resistance in the macrocell corrosion model are provided in the Appendix. Application of Eq. [2-17] for the macrocell corrosion model provides a charge transfer resistance value of 250Ω for a 10-cm [3.94-in] radius anode and concrete ionic resistivity of $10 \text{ k}\Omega\text{-cm}$. The estimated value of the charge transfer resistance is approximately 1.4Ω with an oxygen diffusivity of $10^{-5} \text{ cm}^2/\text{sec}$. The charge transfer resistance is much less than one percent of the electrolyte resistance, consistent with Newman's approach to ignore the charge transfer resistance. This further explains the resemblance between the theoretical disk electrode system and the macrocell corrosion model for the liner-rebar-concrete system and that c is approximately 4.

2.7 Thermodynamic and Corrosion Analysis

Corrosion rates to estimate the corrosion area were computed using OLIAnalyzer Studio (OLISystems, Inc., 2013; Gerbino, 2006). This software was used to derive polarization curves and corrosion rates as a function of pH. Measured hydrated cement pore solution compositions were compiled from published literature. Typically, pore solutions are expressed from hydrated cement samples by triaxial compression using a specially designed high pressure steel die. The pore solution compositions reported in the literature are listed in Table 2-2.

Table 2-2. Summary of Measured Hydrated Cement Pore Solution Composition (moles/Liter) in Published Literature

Species	Average of Data for Specimens Cured for 476 and 569 Days*	Data for Standard Portland Cement†	Average of Data for Cement A and B Specimens‡	Average of Data for Specimens Cured for 6 Months and 1 Year§
Na ⁺	0.1249	0.06525	0.1255	0.1665
K ⁺	0.2376	0.1611	0.3735	0.2633
Ca ²⁺	0.001850	0.002246	0.001825	0.001250
Mg ²⁺	na	8.229×10^{-6}	na	na
Si ⁴⁺	3.45×10^{-4}	2.136×10^{-4}	na	na
Al ³⁺	2.470×10^{-4}	1.853×10^{-4}	na	na
SO ₄ ²⁻	0.01270	na	0.0121	0.0163
OH ⁻	na	na	0.4955	0.3900

na = not applicable

*Rothstein, R., J.J. Thomas, B.J. Christensen, and H.M. Jennings. "Solubility Behavior of Ca-, S-, Al-, and Si-Bearing Solid Phases in Portland Cement Pore Solutions As a Function of Hydration Time." *Cement and Concrete Research*. Vol. 32. pp. 1,663–1,671. 2002.

†Andersson, K., B. Allard, M. Bengtsson, and B. Magnusson. "Chemical Composition of Cement Pore Solutions." *Cement and Concrete Research*. Vol. 19. pp. 327–332. 1989.

‡ Constantiner, D. and S. Diamond. "Pore Solution Analysis: Are There Pressure Effects?" *Mechanisms of Chemical Degradation of Cement-Based Systems*. K.L. Scrivener and J.F. Young (eds.). London, United Kingdom: E&FN Spon. 1997.

§Li, X. "Mitigating Alkali Silica Reaction in Recycled Concrete." Ph.D. Thesis. Durham, New Hampshire: University of New Hampshire, Department of Civil Engineering. 2005.

The expert panel suggested that wood could locally lower the porewater pH. Hendrix (2006) summarized information regarding organic acids present in wood as follows:

"The principle constituent of wood is cellulose, a polysaccharide, i.e., a polymer made of sugar molecules joined in long chains. The sugar units contain mildly basic hydroxyl radicals, some of which are combined with acetylated radicals. The acetyl radical comprises approximately 1 to 6 % by weight of dry wood, with more in hardwoods than in softwoods. Most woods are slightly acidic, with a pH of 3 to 6. Acetic acid from acetyl groups is the most prevalent acid in wood, but other organic acids, including formic, propionic and butyric acids can also contribute to acidic conditions. Different woods vary in the ease with which the acetyl is hydrolyzed to acetic acid. Therefore, depending on the type of wood and the initial acid and moisture contents, woods can vary appreciably in their corrosivity to metals. In a given wood, the rate of formation of acetic acid depends on the temperature and moisture content of the wood."

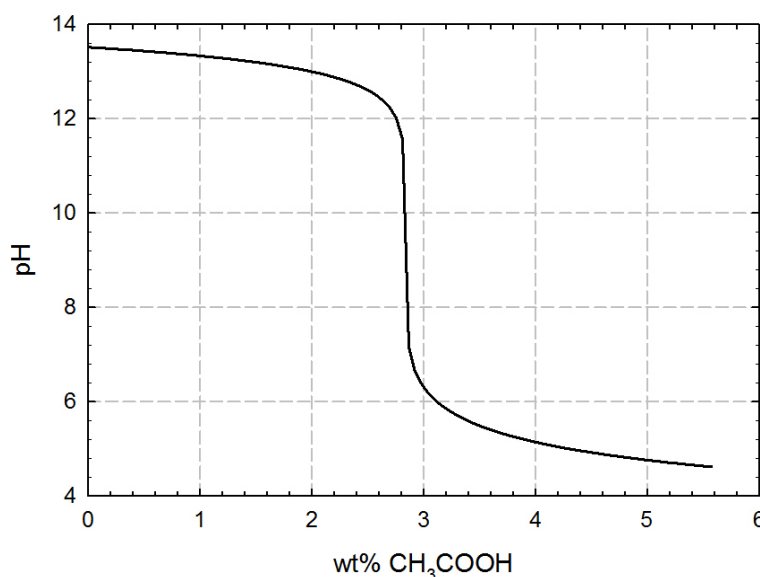
Cement pore solution compositions have been reported in the literature (Andersson, et al., 1989; Constantiner and Diamond, 1997; Li, 2005; Rothstein, et al., 2002). The composition Constantiner and Diamond (1997) measured is similar to the other published values and was selected as the reference pore solution composition for the corrosion analysis. The composition from Constantiner and Diamond (1997) was charge balanced using OLIAnalyzer Studio (OLISystems, Inc., 2013). The initial and charge balanced compositions are listed in Table 2-3. The calculated pH for the pore solution is 13.6.

The concrete pore solution pH as a function of acetic acid concentration (in weight percent) calculated using OLIAnalyzer Studio (OLISystems, Inc., 2013) is shown in Figure 2-10.

Table 2-3. Cement Solution Composition (moles/Liter) Used in Corrosion Analysis*

Species	Concentration (moles/Liter)	Concentration (moles/Liter) After Charge Balancing†
Na^+	0.1255	0.1298
K^+	0.3735	0.3862
Ca^{2+}	0.001825	0.001887
SO_4^{2-}	0.0121	0.0121
OH^-	0.4955	0.4955

*Constantiner, D. and S. Diamond. "Pore Solution Analysis: Are There Pressure Effects?" *Mechanisms of Chemical Degradation of Cement-Based Systems*. K.L. Scrivener and J.F. Young (eds.). London, United Kingdom: E&FN Spon. 1997. (Average of measured values for Types A and B cement.)
†OLISystems, Inc. "OLIAnalyzer Studio." Morris Plains, New Jersey: OLISystems, Inc. 2013
<<http://www.olisystems.com/new-streamanalyzer.shtml>> (March 18, 2013).

**Figure 2-10. pH of Cement Pore Solution As a Function of CH_3COOH Concentration (Weight%) Calculated Using OLIAnalyzer Studio (OLISystems, Inc., 2013)**

Based on the above information, it is concluded that acetic acid formed during degradation of the wood can lower the pH of the concrete porewater and cause the establishment of relatively high corrosion rates. Computations were further performed to compute the corrosion rate of iron in concrete porewater with pH lowered by the acetic acid. The computations considered a temperature of 60 °C [140 °F] and negligible oxygen. The pH was varied from 4 to 10 by adjusting the amount of acetic acid in the system. The calculated current density and corrosion rate results are summarized in Figure 2-11. The corrosion rates are consistent with the order of magnitude corrosion rates inferred from the operational experience. Focusing on the maximal corrosion rates, a 1-cm [0.39-in] thick liner would corrode through in 10 years if the pH was 4; in 100 years if the pH was 7; and in 1,000 years if the pH was 10. The estimated liner corrosion rates by Dunn, et al. (2011), ranging from 0.3 mm/yr to 0.5 mm/yr [12 to 20 mil/yr], correspond

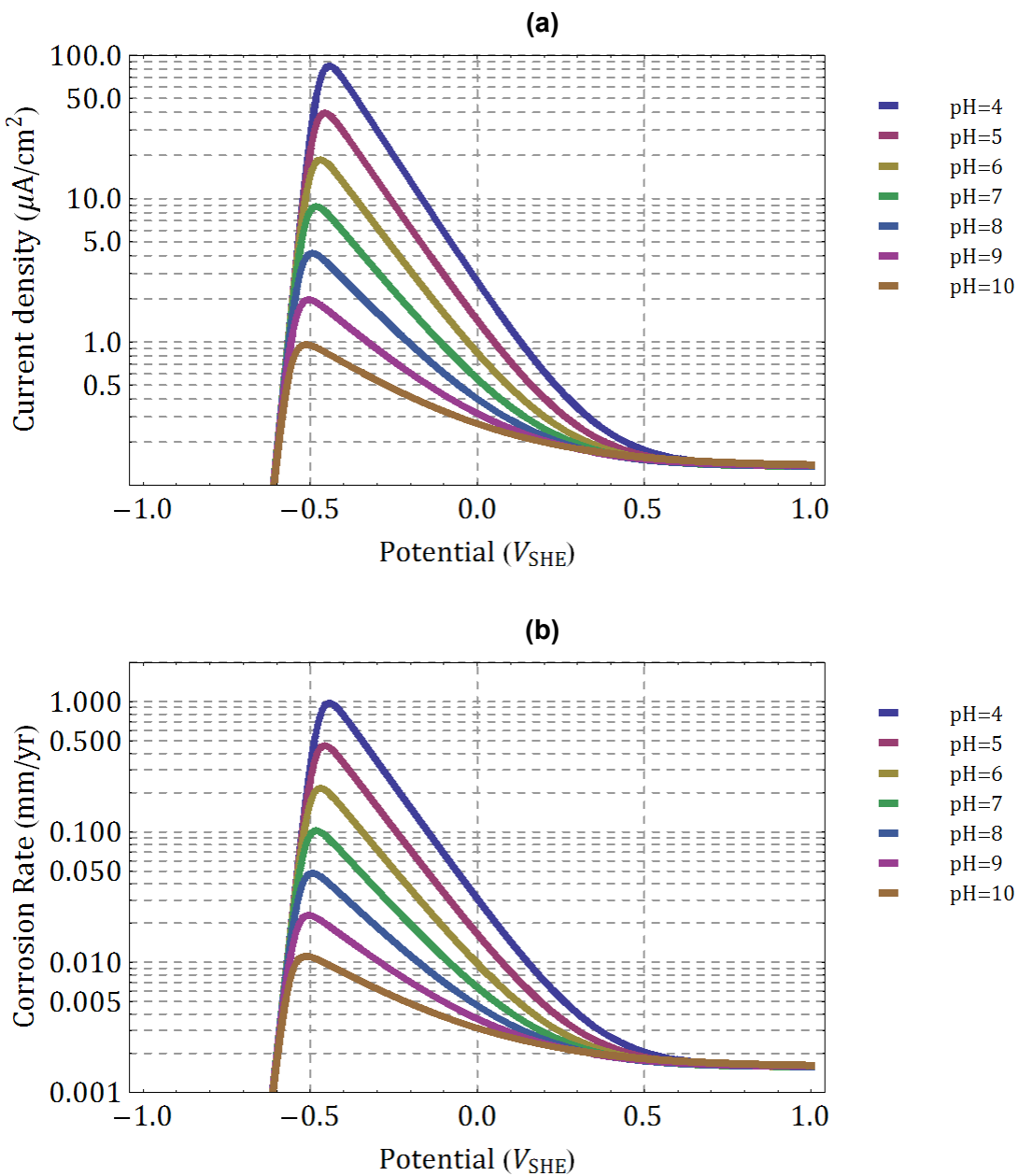


Figure 2-11. Calculated Current Density (a) and Corrosion Rate (b) of Iron in Concrete As Functions of Electrode Potential and pH

to the calculated corrosion rates at a pH from 5 to 6 in Figure 2-11(b). Therefore, the macrocell corrosion mechanism proposed by the expert panel is feasible. In the Monte Carlo analysis in Section 2.8, it is assumed that the pH ranges from 4 to 7. Lower values of the pH would result in fast corrosion rates and liner penetration is less than 10 years, which has not been observed. Higher values of the pH above 7 would result in liner penetration in times greater than 100 years, which is beyond the time of interest.

A question of interest is whether a low pH can be sustained in the long term, causing iron to corrode at a relatively high rate for years. Hydrolysis of ferrous iron is an additional potential source of hydrogen ions, keeping the pH low, and self-promoting iron corrosion. Experimental testing is needed to address the question on whether active corrosion can be sustained for extended periods.

If an acidic solution is developed, this solution is expected to be constrained to the region where wood is in close contact with the liner. Pabalan, et al. (2011) evaluated the potential effect of boric acid leakage from spent fuel pools on the degradation of concrete support structures and rebars. Computations of boric acid diffusive and advective transport were performed to determine the penetration of acid fronts. Pabalan and Chiang (2012) analyzed a system of boric acid flow through a crack, and diffusive penetration of the acid front into concrete in a direction perpendicular to the crack and to the advective flow direction. Pabalan and Chiang (2012) concluded that diffusive propagation of the acid front into the concrete is slow, taking decades to penetrate a few centimeters into the concrete. It is conjectured that a similar rate will hold true for the liner corrosion problem. The acidic solution is highly unlikely to spread beyond the acidity source in a few decades, due to the slow diffusion of hydrogen ions and their reaction with hydroxides in the concrete. In this sense, the contact area between the liner and the foreign wood defines a maximum corrosion surface.

2.8 Estimates of Corrosion Damage Areas

The approach to estimate the liner damage area is explained in this section. A Monte Carlo approach was adopted to compute the damage area. In the Monte Carlo approach, the corrosion damage area is computed as functions of independent parameters, using a deterministic equation. The deterministic inputs are sampled from distribution functions, and the corrosion damage area is computed. This process is repeated multiple times, resulting in multiple outputs of the corrosion damage area. Statistics and numerical joint distributions (e.g., joint distribution for the corrosion rate and damage area) are computed from the populations of outputs.

It was previously argued, in Section 2.5, that the extent of moisture expected to remain in the concrete is high, given the 1.2-m [3.94-ft] thick concrete wall. A reasonable value for the concrete ionic resistivity under those conditions is 10 k Ω -cm, consistent with views in the expert panel report (SNL, 2011). Figure 2-6 indicates that the deviation from the straight line, Eq. [2-15], due to uncertainty/variability in kinetic, oxygen diffusion, and rebar coverage parameters, is within 20 percent for the case $\rho=10$ k Ω -cm. Based on a limiting model, the constant c in Eq. [2-15] has a theoretical value of 4 (see Section 2.6). To account for uncertainty or variability in the oxygen diffusion coefficient and rebar coverage, c is assumed to range from 4 to 4.8. The concrete ionic resistivity is sampled from a triangular distribution with ends at 10 k Ω -cm and 50 k Ω -cm and mode at 20 k Ω -cm. The average of this distribution is 26.7 k Ω -cm, the median is 25.5 k Ω -cm, and the standard deviation is 8.5 k Ω -cm. The assumed cumulative distribution is presented in Figure 2-12. The resistivity distribution was selected to calibrate to observations of liner corrosion, discussed by Dunn, et al. (2011). These authors reported corrosion rates on the order of 0.5 mm/yr [20 mil/yr] and damage by corrosion on the order of 1 to 10 cm 2 [0.16 to 1.6 in 2].

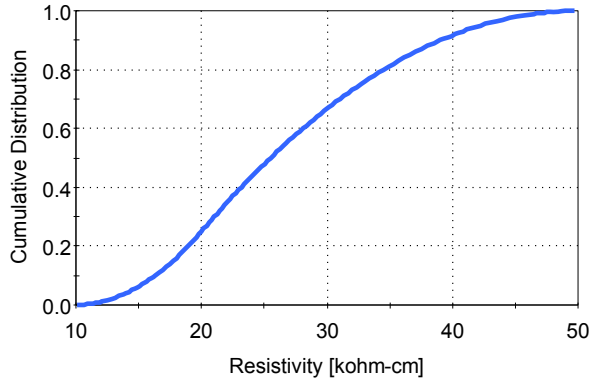


Figure 2-12. Assumed Cumulative Distribution for the Concrete Ionic Resistivity

Figure 2-11, the maximum anodic current density as a function of pH is computed as (equation obtained by curve fitting)

$$i_{max} = 1 \frac{\mu A}{cm^2} \exp(7.5 - 0.776 pH - 0.0021 pH^2) \quad [2-18]$$

The electrode potential at the anode at which the maximum is attained is computed as (equation also derived by curve fitting)

$$E_{max} = (-0.382 - 0.017 pH - 0.00038 pH^2) \times 1 V_{SHE} \quad [2-19]$$

The pH is sampled from a triangular distribution with extremes at 4 and 7, and a mode at 6. From the polarization curve data in Figure 2-11(b) and Eq. [2-18], pH=4 corresponds to a corrosion rate of 0.98 mm/yr [39 mil/yr]; pH=6 to 0.2 mm/yr [7.9 mil/yr]; and pH=7 to 0.1 mm/yr [3.9 mil/yr].

The distal electrode potential (i.e., the electrode potential at a far distance from the anode, taken at a radius of 8 m) is computed as

$$E_{distal} (\text{mV vs SHE}) = E_o - 58.072 \text{ mV} \ln \left(\frac{i_{pas}}{i_{O_2}^0} \right) \quad [2-20]$$

The parameter E_o is a function of the oxygen concentration, which is a function of the oxygen diffusion and anode potential. The average value of E_o , derived from simulations with high ionic resistance and low diffusion coefficient, is 96.4 mV. E_{distal} is calibrated to corrosion potentials measured in slightly deaerated concrete. Under such conditions the corrosion potential is expected to range from -200 mV to -100 mV versus standard calomel electrode (Bertolini et al., 2004), which is approximately equivalent to 50 mV to 150 mV versus SHE. This calibration is accomplished by setting $i_{pas} = 0.01 \mu\text{A}/\text{cm}^2$, and sampling $i_{O_2}^0$ from a triangular distribution with ends at 0.0045 and 0.025 $\mu\text{A}/\text{cm}^2$, and mode at 0.015 $\mu\text{A}/\text{cm}^2$. The average value $E_o = 96.4 \text{ mV}$ was also used in the calibration.

The driving potential is computed as

$$\Delta E = E_{distal} - E_{max} = \\ 0.0964 V - 0.058 V \ln\left(\frac{i_{pas}}{i_{O_2}^0}\right) + (0.382 + 0.017 pH + 0.00038 pH^2) \times 1 V \quad [2-21]$$

Figure 2-13 shows a distribution of the driving potential derived with the Monte Carlo method. The average, median, and mode of the driving potential are approximately the same value equal to 580 mV.

The approach to estimate the corrosion damage area is as follows. The current density at the anode equals the net current divided by the anode area, for example

$$i_{max} = \frac{I}{\pi r^2} = \frac{c r \Delta E}{\pi r^2 \rho} = \frac{c \Delta E}{\pi r \rho} \quad [2-22]$$

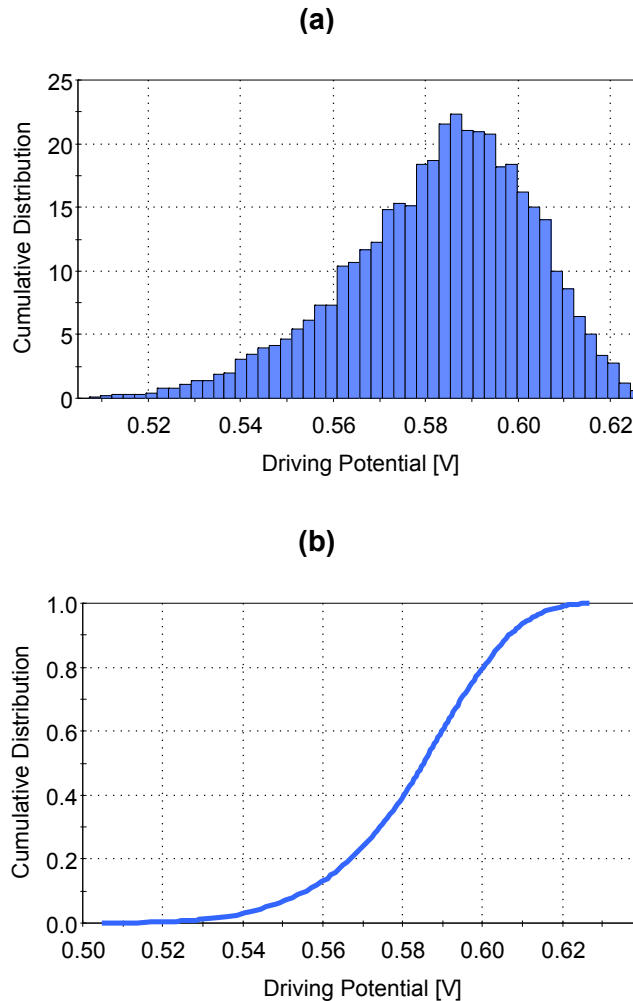


Figure 2-13. Numerical Distribution of the Driving Potential Derived With Monte Carlo Analysis. (a) Probability Distribution and (b) Cumulative Distribution.

from which the anode radius is computed as

$$r = \frac{c \Delta E}{\pi \rho i_{max}} = \frac{c \kappa \Delta E}{\pi i_{max}} \quad [2-23]$$

and the anode area is then computed as $A = \pi r^2$

$$A = \frac{(c \kappa \Delta E)^2}{\pi (i_{max})^2} \quad [2-24]$$

Assuming a 1-cm [0.39-in] thick liner, the time for through-wall corrosion is computed as

$$t = \frac{10 \text{ mm}/(0.0116 \text{ mm/yr})}{i_{max}/(1 \mu\text{A}/\text{cm}^2)} \quad [2-25]$$

In Eq. [2-25], the equivalence $1 \mu\text{A}/\text{cm}^2$ (current density) = 0.0116 mm/yr [0.46 mil/yr] was used (Warkus, et al., 2006).

In the Monte Carlo model, the time of interest was considered to be less than 100 years. Also, the corrosion damage area is expected to be physically bound. As described in Section 2.7, it is unlikely that corrosion damage will extend beyond the area of contact of the foreign wood and the liner. For example, in the Beaver Valley Unit 1 through-wall corrosion case, the corroded area was $2.5 \text{ cm} \times 1.0 \text{ cm}$ [0.98 in \times 0.39 in], but the foreign piece of wood was of dimensions $5 \text{ cm} \times 10 \text{ cm} \times 15 \text{ cm}$ [1.97 in \times 3.94 in \times 5.9 in]; i.e., much larger than the size of the corrosion patch. Similarly, in the North Anna Unit 2 case, the corrosion caused a hole on the liner 0.635-cm [0.25-in] diameter. The underlying piece of wood was of dimensions $10 \text{ cm} \times 10 \text{ cm} \times 1.8 \text{ m}$ [3.9 in \times 3.9 in \times 5.9 ft], again larger than the corrosion damage. Monte Carlo cases with large corrosion damage are interpreted to mean that corrosion is limited by the size of the contact between the wood and the liner, and not by the driving potential and concrete ionic resistance.

Figure 2-14 includes a scatter plot of the liner corrosion area versus pH and conditional cumulative functions of the corrosion area as a function of the pH range. If the pH is low, the corrosion rate would be higher, and the corrosion damage would be expected to be localized. On the other hand, higher pH is associated with lower corrosion rates and, thus, more widespread corrosion. The corrosion rate in the analyses ranges from 0.1 to 1 mm/yr; thus, liner penetration would occur after few decades up to 100 years of reactor operation.

Figure 2-15 displays a scatter plot of the corrosion area versus the concrete ionic resistivity, and conditional cumulative distribution curves for the corrosion area as a function of the resistivity range. From Eq. [2-24], the area is proportional to κ^2 and $\kappa=1/\rho$. Thus, the area is inversely proportional to the square of the resistivity, ρ^2 , and this explains why larger corrosion areas in Figure 2-15 correspond to lower values of the concrete ionic resistivity.

The conditional distribution function in Figure 2-16 is the combined distribution function used in the leak rate computations in Chapter 3. The combined distribution accounts for uncertainty in the corrosion rate and concrete resistivity, as well as uncertainty in other parameters of the Monte Carlo model such as the driving potential and the resistivity constant c .

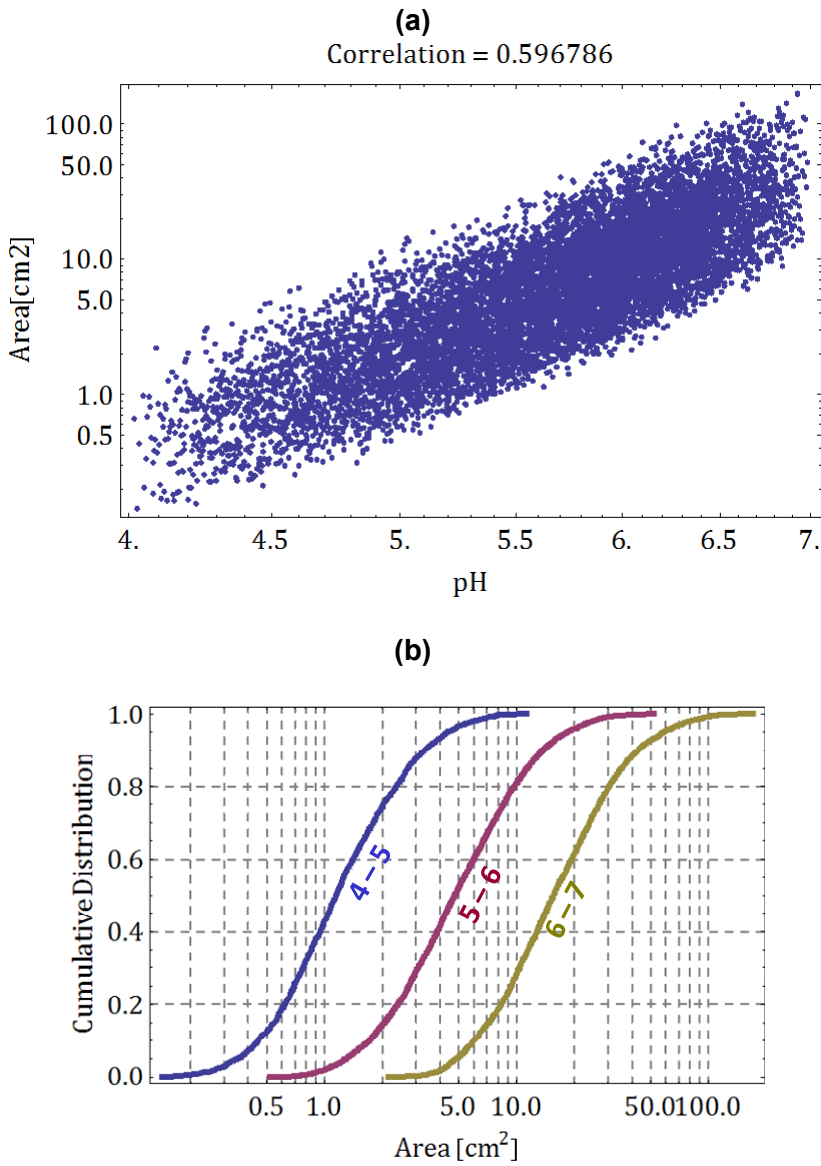


Figure 2-14. Estimates of Corrosion Damage Area From the Monte Carlo Analysis.
(a) Scatter Plot of the Area Versus the pH and (b) Conditional Cumulative Distribution Function for the Corrosion Damage Area As a Function of the pH (the pH Range is Indicated by Labels in the Figure).

The corrosion area in Figure 2-16 is predicted to attain large values, based on a model that does not explicitly consider limitations imposed by the contact between the wood and the liner. Instead, the main limitations are imposed by the concrete ionic resistivity, the driving potential, and the corrosion rate associated with an assumed solution pH. Large corrosion areas in Figure 2-16 are interpreted to mean that, in reality, the contact between the wood and the liner will control the area of damage. If the contact area is small, then the equivalent radius, r , is small, and Eq. [2-23] implies that the ratio, $\Delta E/i$, and ΔE in specific, would have to be small

$$\frac{\pi r}{c \kappa} = \frac{\Delta E}{i} \quad [2-26]$$

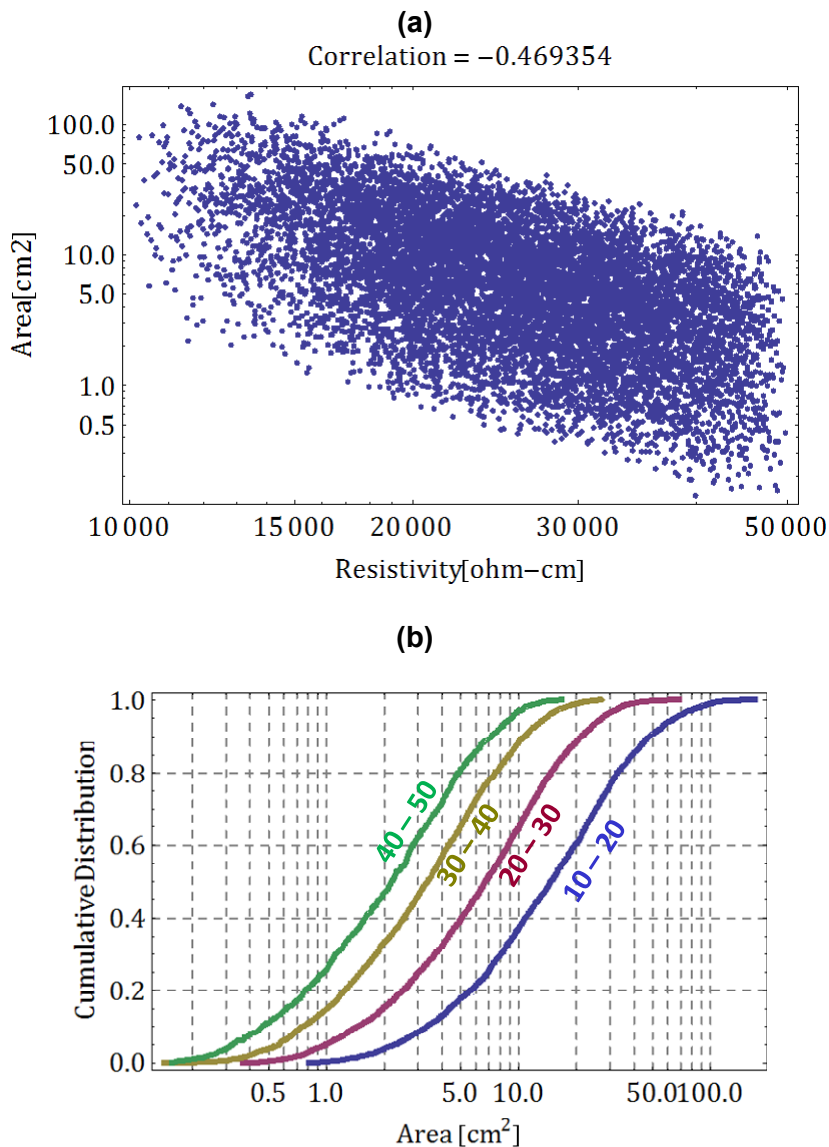


Figure 2-15. Estimates of Corrosion Damage Area From the Monte Carlo Analysis.
(a) Scatter Plot of the Area Versus the Concrete Ionic Resistivity and (b) Conditional Cumulative Distribution Function for the Corrosion Damage Area As a Function of the Resistivity (the Resistivity Range (in $k\Omega\text{-cm}$) is Indicated by Labels in the Figure).

Small ΔE implies small values of i and the corrosion rate. In the limit when the contact radius becomes very small, the corrosion rate becomes negligible (i.e., the liner would exhibit passive corrosion).

In the derivation of the cumulative distribution in Figure 2-16, it was assumed that

- The anode is at a constant potential
- The chemistry in the anode region is uniform
- The corrosion rate is uniform

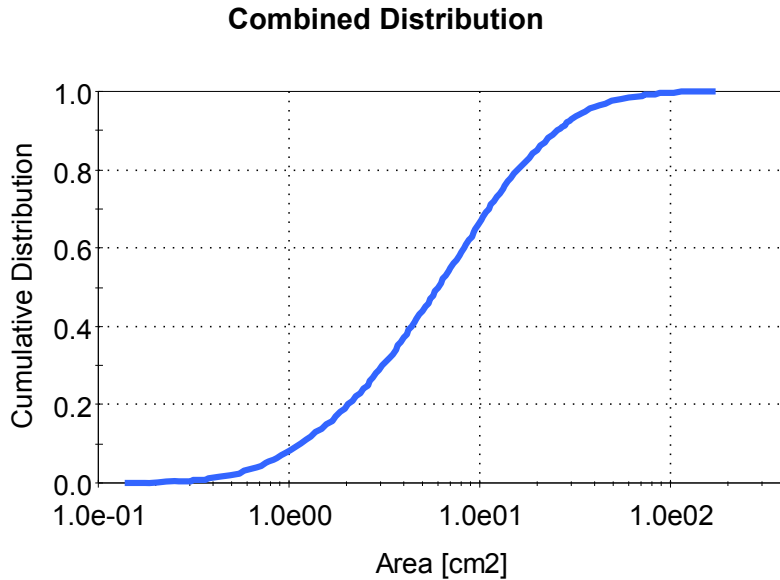


Figure 2-16. Combined Distribution for the Corrosion Area From the Monte Carlo Analysis

In reality, the chemistry in the anode region is expected to be variable, which will result in a non-uniform corrosion rate, with a distributed electric potential. The corrosion front will propagate in a non-uniform manner, and the leading front will cause the through-wall corrosion. Corrosion damage will propagate with time up to a size limited by the contact area between the wood and the liner. The size of the corrosion damage in Figure 2-16 is an overestimate of the corrosion area, because the wood-liner contact area was implicitly assumed to be large, and the driving potential, ΔE , was assumed to attain large values. More accurate estimates of the corrosion area, accounting for realistic wood-liner contact areas, are expected to result in smaller areas in the upper tail of the distribution than in Figure 2-16. On the other hand, more accurate estimates of the anode potential and its distribution are expected to result in smaller estimates of the anode current density and smaller corrosion rates, which may yield later times for through-wall failure. Results in Figure 2-16 are dependent on the assumed values of the concrete ionic resistivity (which is highly uncertain) and corrosion rates as functions of pH and electrode potential (which are also uncertain).

The diagram in Figure 2-17 is a concept of the propagation of the corrosion front, proposed to estimate in detail the time of through-wall corrosion, and the growth of the corrosion area. It is proposed to perform computations in a stage-wise manner, using the steady-state equations for mass and charge balance presented in this chapter. In a more detailed approach, assumptions and simplifications still need to be made in regards to the initial size of the active zone, the pH distribution on the anode region and any evolution with time, the surface of the corrosion front, and the anode current density as functions of pH and electrode potential, $i_a(pH, E)$. Time snapshots based on steady-state solutions could be pursued, and later abstracted to estimate the rate of propagation of the center of the corrosion front. Simple geometries could be considered to estimate the propagation of the corrosion front and subsequent growth of the corrosion area. The advantage of a more detailed approach is that the estimates of the rate of growth of the corrosion area would arise, as opposed to simplified estimates in this chapter.

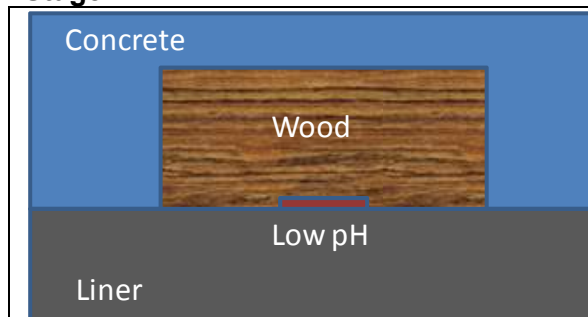
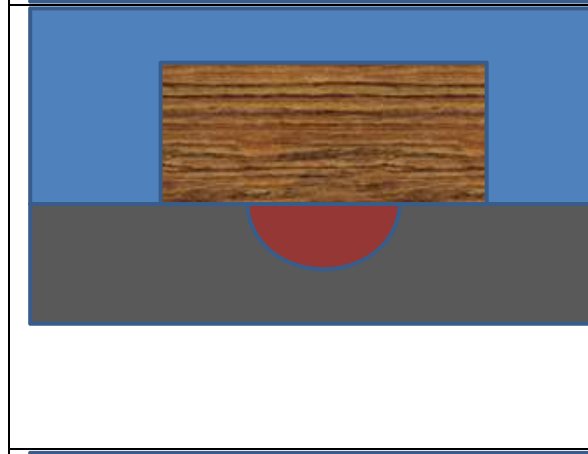
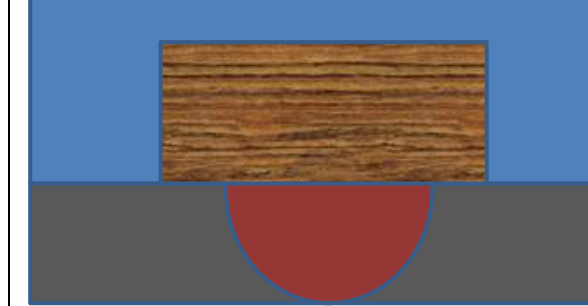
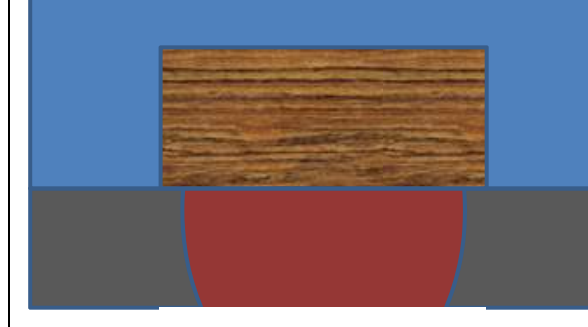
Stage	Comment
 <p>Concrete Wood Liner Low pH</p>	<p>The wood is initially in contact with the liner. A region of low pH develops, and the liner becomes activated. The following equation could be used to estimate the initial corrosion rate</p> $i_a(pH, E) \pi r^2 = c \kappa r (E - E_o)$ <p>r — initial radius of the active zone E — initial potential, estimated as the corrosion potential in highly deaerated concrete porewater E_o — far corrosion potential</p>
	<p>A corrosion front develops. A pH gradient is likely to develop. It is conjectured that a relationship such as the following may hold valid</p> $\int i_a(pH, E(r)) dS = c \kappa \int (E(r) - E_o) dr$ <p>dS is a surface differential along the corrosion front surface, and r is a radial coordinate measured along the corrosion front surface, from the center to the edge. Simulations using a differential equation solver will be needed to verify whether such equation holds. Solution to the mass and charge balance differential equations will yield $i_a(pH, E(r))$ for an assumed pH distribution on the anode. Simple surfaces such as sphere or cone sections may need to be considered for the stylized computations in the differential equation solver.</p>
	<p>The corrosion front becomes through-wall. At that point the corrosion of the liner may become detectable. If not detected, the damage area may continue growing.</p>
	<p>The corrosion area grows with time, up to a point constrained by the contact area with the wood.</p> <p>The corrosion front surface may be conceptualized as a section of a cone for stylized computations with the differential equation solver.</p>

Figure 2-17. Conceptualized Stages in the Propagation of a Corrosion Front Leading to Through-Wall Corrosion

providing single values for the penetration time and the maximum area compromised by corrosion. The detailed approach described in Figure 2-17 was beyond the scope of this

project. Also, if the method in Figure 2-17 is successful, rates of growth of the corrosion area would still depend on assumptions made on the pH distribution and the dependence of the anodic current density on the pH and electrode potential, which will require experimental verification.

2.9 Discussion —Corrosion Model

Thermodynamic and corrosion simulations indicate corrosion rates ranging from 0.01 mm/yr to 1 mm/yr [0.39 mil/yr to 39 mil/yr] considering a representative concrete porewater composition, with pH controlled by acetic acid. The results obtained from this work are consistent with the estimated corrosion rates of 0.3 to 0.5 mm/yr [12 to 20 mil/yr] by Dunn, et al. (2011). Testing could be used to investigate the dependence of corrosion rates on the pH, applied potential, and time, in relevant concrete porewater chemistries. Results of the macrocell corrosion model and thermodynamic simulations are consistent with (i) the range of corrosion rates leading to through-wall corrosion that have been observed, (ii) the range of ionic resistivity that the expert panel suggested applies to the containment building concrete, and (iii) the range of corrosion areas in the detected instances of through-wall corrosion. Because of this consistency, it is concluded that macrocell corrosion is a feasible process explaining the instances of through-wall liner corrosion.

It is unlikely that damage will extend beyond the contact area between the foreign wood and the liner, as any acidic porewater front would propagate by diffusion, which is a slow process, and also react with hydroxides in concrete. Clear differentiation of the water chemistry is required to separate the anode and cathode in the macrocell. Such separation can be attained by tight contact between the wood and the liner. If the contact was not tight, the local porewater composition would be dominated by the bulk porewater chemistry, which passivates carbon steel. Therefore, the contact area between the wood and the liner defines an upper bound for liner area compromised by corrosion.

A steady-state model was developed that disregards propagation aspects (propagation of the corrosion area and propagation of the corrosion front), and variability in the porewater chemistry near the active corroding area on the liner (i.e., the anode). Limitations imposed by the limited contact area between the wood and the liner were also ignored. The most important independent variables controlling the net ionic current in the model are the concrete ionic resistivity, the driving potential (i.e., the difference between the far cathode potential and anode potential), and the anode radius. Variability in kinetic parameters of reactions (passive dissolution and oxygen reduction), oxygen diffusion coefficient, and rebar coverage have a relatively small effect on the net ionic current in the system (which is related to the corrosion rate and the area of the liner that could undergo localized corrosion), provided the concrete ionic resistivity (ρ) is around 10 k Ω -cm [such resistivity magnitude is inferred from the expert panel report (SNL, 2011)]. The macrocell liner-concrete system can be very well approximated by the idealized system of a disc electrode with a counter electrode located at infinity. The detailed steady-state solution to the charge and mass balance equations in the liner-concrete-rebar system is consistent with this theoretical limit.

Synthesis equations were derived to estimate the liner damage area affected by corrosion. A Monte Carlo model was implemented to account for key uncertainties (e.g., uncertainty in the concrete ionic resistivity, pH, and driving potential) and derive data populations from which statistics on the corrosion area are computed. These synthesis equations were coupled to the leak rate model to provide input damage areas to leak rate computations. From the Monte

Carlo simulations, the concrete ionic resistivity and solution pH are the most important parameters determining the corrosion damage area. Ranges of damage areas were estimated considering a range of concrete ionic resistivity between 10 and 50 kΩ-cm, and pH between 4 and 7. Larger extent of damage is computed when smaller values of the concrete ionic resistivity are selected. The range of concrete ionic resistivity considered in the computations was selected to be consistent with through-wall liner corrosion areas detected in the incidents at Beaver Valley Unit 1 and North Anna Unit 2 nuclear power plants, and also consistent with recommendations from the expert panel report.

The following bullets summarize main conclusions of the corrosion analysis, assumptions and limitations of the analysis, and potential additional studies to reduce uncertainties. A more rigorous treatment of corrosion may result in slower estimates for the rate of corrosion, as well as slower rates for lateral propagation.

Main Conclusions of the Corrosion Analysis

- The macrocell corrosion process proposed by the expert panel well explains the observed corrosion rates and corrosion area on the containment liner
- Macrocell corrosion requires a clear differentiation between the anode and cathode. Differentiation in the local-to-the-anode and bulk porewater composition can be sustained by tight contact between the foreign wood and the carbon steel liner. It is unlikely for the corrosion damage to extend well beyond the area of contact between the wood and the liner.
- The concrete ionic resistivity and the corrosion rate (which is a function of the porewater pH) are the dominant parameters controlling the corrosion area
- In the range of resistivity on the order of 10 kΩ-cm, parameters such as the passive current density, the exchange current density for oxygen reduction, and the amount of rebar play a secondary role on the determination of the net current conducted through the concrete (which is related to the corrosion rate at the anode and the area of the anode)
- The model predicts corrosion areas on the liner ranging from few square centimeters to tens of square centimeters and larger, conditional on the assumed values of the ionic resistivity. Large damage area estimates are associated with low values of the concrete ionic resistivity or low values of the corrosion rate. Larger estimates of the corrosion area are obtained by considering lower values of the ionic resistivity.
- Large corrosion areas calculated by the model only indicate that the contact area between the wood and the liner is the actual upper bound on the corrosion area (because the corrosion damage is unlikely to extend beyond this area of contact)
- If the contact area is small and the resistivity of the concrete is large, the liner is likely to remain passive

Analysis Assumptions and Limitations

- The system is modeled as steady-state (corrosion propagation is ignored)

- Time dependencies of corrosion rates, porewater compositions, corrosion product buildup and feedback on corrosion rates, as well as heterogeneities in the anode are ignored
- Constraints imposed by limited contact area between the foreign wood and the liner are disregarded
- Fast pathways for the supply of oxygen (e.g., cracks on the concrete or existing penetrations in the concrete structure) are not considered
- The thermodynamic simulations considered a single, representative, concrete porewater composition
- The Monte Carlo estimates of the damage area depend on assumed values of the concrete ionic resistivity and predictions of the corrosion rate as a function of pH and the driving potential
- The question of initiation and likelihood of localized corrosion by the macrocell process is not analyzed. The results of the analysis are conditional on the system establishing the appropriate conditions for initiating and sustaining the macrocell process. In particular, the questions on the likelihood for foreign wood to come into tight contact with the liner, and the extent of the possible contact are not analyzed.

Potential Additional Studies to Reduce Corrosion Model Uncertainties

- Measure the corrosion rate as a function of the concrete porewater composition, pH, and electrode potential, and evolution of the corrosion rate as a function of time (buildup of corrosion products is expected to change corrosion rates)
- Measure the concrete ionic resistivity of representative concrete in contact with the steel liner
- Estimate the likelihood for frame wood to contact the liner as a function of the concrete volume in the containment building
- Estimate the distribution of contact area of the foreign wood and the carbon steel liner
- Develop a dynamic model to track propagation of corrosion

3 LEAK RATE MODEL

Computations in this chapter are aimed at estimating gas (water vapor and air) leak rates from the containment building in case of a loss-of-coolant accident (LOCA) and a steel liner compromised by through-wall corrosion. The synthesis model to estimate the damage area by corrosion, discussed in Chapter 2, is used to define the liner leak area. Sensitivity analyses are performed to identify factors controlling leak rates.

3.1 Approach

A mass and energy balance model is developed to estimate the pressure, temperature, and mass of vapor in the containment building (referred to as compartment A), considering temperature and pressure transients typically included in the Updated Final Safety Analysis Reports (UFSARs) as part of analyses of containment response to LOCAs. The mass balance model is coupled to a 2-dimensional gas flow model to compute gas transport through a narrow space (space between the liner and the concrete, referred to as compartment B) until an outlet to the atmosphere is intercepted. The outlet to the atmosphere is postulated to be an existing penetration through the concrete such as those arising from inadequate bonding of the concrete or to piping or airlocks. Other potential pathways, such as cracks through the containment concrete, were disregarded because through-wall cracks were considered unlikely and uncorrelated to the location of the foreign wood in contact with the liner. Cracks could develop in case of extreme pressures, under beyond design basis accident conditions. To keep the analysis focused, only pressures associated with design basis accidents are considered in this report. The concrete is unlikely to crack under design basis accident pressures. The gas flow model is used to compute the leak rate to the atmosphere, which in turn provides feedback to the mass balance model to determine the amount of vapor in the containment building and its temperature. Ideal gas equations are used to compute gas density, mass, pressure and temperature. Energy losses are disregarded, and the gas in the narrow space (i.e., compartment B) is assumed to be at the same temperature as the gas in the containment building.

A Reactor Containment Building (RCB) integrated leakage test (Type A Leak Rate Test) from North Anna Unit 2 (Beaver Valley Power Station, 2009) was used to calibrate the model to estimate parameters such as the aperture of the narrow space between the liner and the concrete. Sensitivity analyses are performed to understand contributions from uncertain parameters to the leak rate.

3.2 Mass and Energy Balance Model

Figure 3-1 is a simplified schematic of the containment building in a pressurized water reactor (PWR). For the mass and energy balance model, the system is conceptualized into four compartments depicted in Figure 3-2. Compartment A is the main containment volume. It represents the volume inside the liner in Figure 3-1. Compartment B is the volume between the liner and the concrete. This volume is accessible only in case of through-wall corrosion of the liner. In case of a LOCA, vapor would flow through this constrained space until an outlet is intercepted, assuming that the concrete is impermeable. The outlet is conceptualized as an existing penetration through the concrete, such as those penetrations arising from airlocks, pipes, or tubes and improper

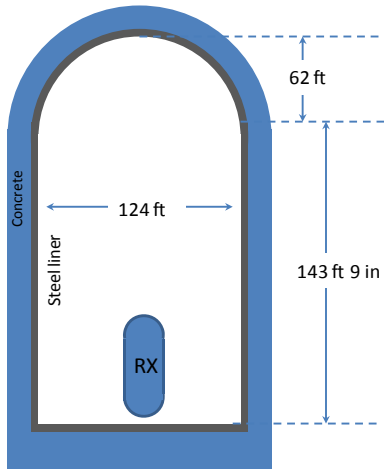


Figure 3-1. Schematic of a Pressurized Water Reactor Containment Building

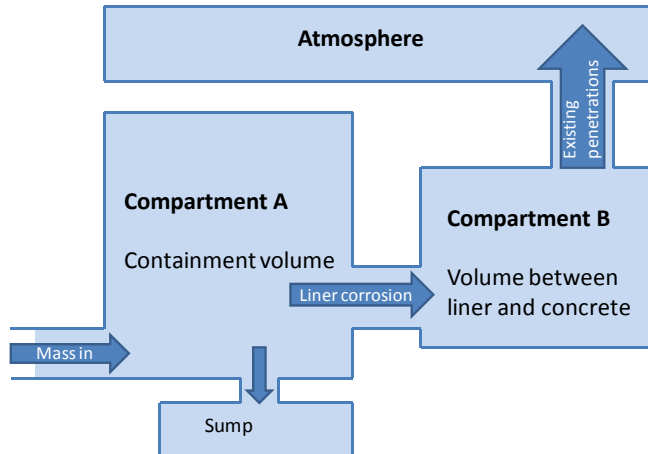


Figure 3-2. Four Compartment Concept for the Mass and Energy Balance Model

bonding of the concrete. The third compartment labeled as “sump” in Figure 3-2 is used to account for vapor condensation and the action of a emergency core cooling system (ECCS), modeled as mass and energy removal from Compartment A. The fourth compartment is the atmosphere, which is used to aggregate the mass of vapor leaked.

Inputs to the mass and energy balance are postulated post LOCA pressure and temperature transients, assuming no-leakage from the containment building. These transients are used to compute the mass of vapor released into the system, and the effect of the ECCS. Stylized transients from the ASTM D 3911-03 standard (ASTM International, 2003), PWR containment, were used as input to computations in this report. These transients are comparable to design basis accident transients considered in UFSARs as part of analyses of containment response to LOCAs. In these analyses, pressures are typically considered to rise from approximately 1 to 4 atm [14.7 to 58.8 psi], and temperatures from approximately 320 to 420 K [116 to 296 °F], over periods on the order of 100 seconds. Temperatures and pressures decrease at later times due to the ECCS action. Transients are typically specified for a time span of 10^6 seconds.

Peak temperatures and pressures in the ASTM standard are above these ranges; thus, the stylized ASTM transients appear to bound transients in UFSARs analyses of containment response to LOCAs. Figure 3-3, reproduced from NUREG/CR-6914, Appendix C, Figure 3 (Los Alamos National Laboratory, 2006), is an example of a typical temperature transient.

The rate at which vapor mass is inserted into Compartment A is computed as

$$\frac{dm}{dt}(\text{to A}) = \dot{m}_{to\ A} = \frac{V}{R} \frac{d}{dt} \left(\frac{P}{T} \right) \quad [3-1]$$

where V is the Compartment A volume, R is the individual gas constant in units of J/kg-K (equal to 461 J/kg-K [2760 ft-lb/slug-°R] for water vapor; equal to 287 J/kg-K [1720 ft-lb/slug-°R] for air; Moran and Shapiro, 2000), and P and T are the input pressure and. Note that the time derivative of the ratio P/T can be negative as a result of the action of the ECCS. In that case, $\dot{m}_{to\ A} = 0$, and

$$\frac{dm}{dt}(\text{to sump}) = \dot{m}_{to\ sump} = -\frac{V}{R} \frac{d}{dt} \left(\frac{P}{T} \right) \quad [3-2]$$

Energy into the system is approximated as

$$\frac{dE}{dt}(\text{to A}) = c_p(T) T \dot{m}_{to\ A} \quad [3-3]$$

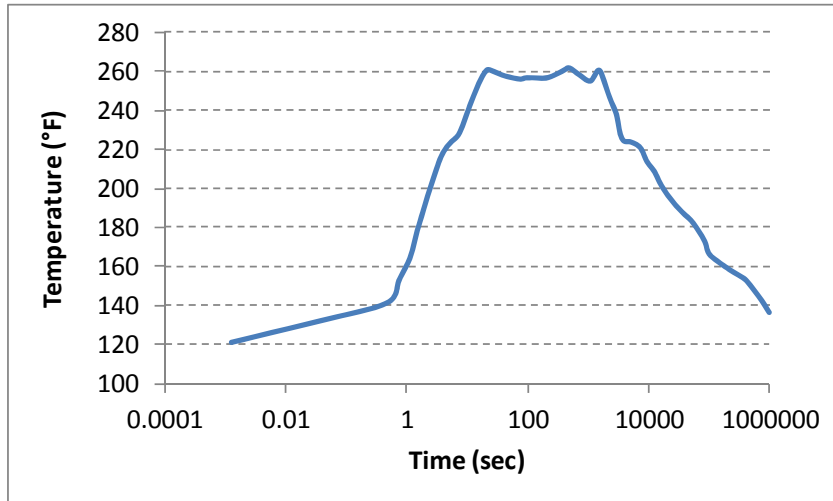


Figure 3-3. Example of Temperature Transient Considered in Analysis of Containment Response Following a Loss-of-Coolant Accident [NUREG/CR-6915, Appendix C, Figure 3 (Los Alamos National Laboratory, 2006)]

where $c_p(T)$ is the constant pressure heat capacity of vapor. If the time derivative of P/T is negative, then $dE/dT(\text{to A})=0$, and

$$\frac{dE}{dt}(\text{to sump}) = c_p(T) T \dot{m}_{\text{to sump}} \quad [3-4]$$

The rate of vapor mass transfer from Compartment A to Compartment B, r_{AB} , and the rate of gas leakage from Compartment B to the atmosphere, $r_{B,atm}$, is computed using a gas flow model discussed in the next section. The mass balance differential equation for the system can be written as

$$\frac{d}{dt} \begin{pmatrix} m_A \\ m_B \\ m_S \\ m_{atm} \end{pmatrix} = \begin{pmatrix} -(\lambda_{A,atm} + \lambda_{AS} + \lambda_{AB}) & \lambda_{BA} & 0 & 0 \\ \lambda_{AB} & -(\lambda_{BA} + \lambda_{B,atm}) & 0 & 0 \\ \lambda_{AS} & 0 & 0 & 0 \\ \lambda_{A,atm} & \lambda_{B,atm} & 0 & 0 \end{pmatrix} \begin{pmatrix} m_A \\ m_B \\ m_S \\ m_{atm} \end{pmatrix} + \begin{pmatrix} \dot{m}_{\text{to A}} \\ 0 \\ 0 \\ 0 \end{pmatrix} \quad [3-5]$$

where the symbol λ represents a fractional release in units of 1/sec, and Table 3-1 describes symbols in Eq. [3-5].

A similar equation to Eq. [3-5] applies to energy conservation:

$$\frac{d}{dt} \begin{pmatrix} E_A \\ E_B \\ E_S \\ E_{atm} \end{pmatrix} = c_p(T_A) T_A \begin{pmatrix} -(\lambda_{A,atm} + \lambda_{AS} + \lambda_{AB}) & \lambda_{BA} & 0 & 0 \\ \lambda_{AB} & -(\lambda_{BA} + \lambda_{B,atm}) & 0 & 0 \\ \lambda_{AS} & 0 & 0 & 0 \\ \lambda_{A,atm} & \lambda_{B,atm} & 0 & 0 \end{pmatrix} \begin{pmatrix} E_A \\ E_B \\ E_S \\ E_{atm} \end{pmatrix} + c_p(T) T \begin{pmatrix} \dot{m}_{\text{to A}} \\ 0 \\ 0 \\ 0 \end{pmatrix} \quad [3-6]$$

The temperature used in the term $c_p(T_A) T_A$ in Eq. [3-6] corresponds to the temperature at the previous timestep. The initial conditions for the system (initial pressure, temperature, energy) are defined by the initial values in the pressure and temperature input transients (e.g., values at

Table 3-1. Description of Fractional Release Symbols

Symbol	Description
$\lambda_{A,atm} = r_{A,atm}/m_A$	Transfer from A to the atmosphere. This direct transfer arises, for example, from defects in seals in airlocks. This direct transfer is set to 0 in computations in this chapter.
$\lambda_{AS} = \dot{m}_{\text{to sump}}/m_A$	Transfer from A to sump. This transfer arises due to the action of the emergency core cooling system (ECCS).
$\lambda_{AB} = r_{AB}/m_A$	Transfer from A to B through the liner corrosion damage. The transfer rate, r_{AB} , is described in Section 3.2.
$\lambda_{BA} = r_{BA}/m_B$	Transfer from B to A. This transfer arises in case the pressure of A drops below B due to the action of the ECCS.
$\lambda_{B,atm} = r_{B,atm}/m_A$	Transfer from B to the atmosphere. The transfer rate, $r_{B,atm}$, is due to gas flow and it is described in Section 3.2.

the initial time in the ASTM D 3911 PWR containment transients). At a timestep i , the coupled system of differential equations is numerically integrated to compute the mass and energy at this new timestep. The temperature of Compartment A at the new timestep, T_A^i , is defined as

$$T_A^i = \frac{E_A^i}{c_v(T_A^{i-1}) m_A^i} \quad [3-7]$$

where c_v is the constant volume heat capacity, the superscript i represents the new timestep, and $i-1$, the previous timestep. The pressure of Compartment A is computed as

$$P_A^i = \frac{R m_A^i T_A^i}{V} \quad [3-8]$$

It is assumed that $T_B^i = T_A^i$. This is justified because (i) the volume of Compartment B is very small compared to Compartment A, and (ii) gas flow is most likely to occur along the liner, which is an efficient thermal conductor. It is assumed that the initial pressure for Compartment B is the atmospheric pressure. The empirical equation in Moran and Shapiro (2000) was used to compute $c_p(T)$ as a function of the temperature. For ideal gases, $c_p - c_v = R$ (Gaskell, 1995). Note that Eq. [3-7] is based on an ideal gas system without heat dissipation. Because the system is modeled as adiabatic, the computed temperature tends to overestimate the actual temperature of the physical system.

Consequently, Eq. [3-8] also overestimates the actual pressure, given the proportionality to the adiabatic temperature. The gas density in Compartment A is

$$\rho_A^i = \frac{P_A^i}{R T_A^i} = \frac{m_A^i}{V} \quad [3-9]$$

The gas density ρ_A is used as boundary condition for gas flow computations through Compartment B.

3.3 Gas Flow Through Compartment B

In case of a LOCA and a liner surface compromised by corrosion, gas could escape to the atmosphere. In this work, it is postulated that the leakage pathway is the constrained space between the liner and the concrete, eventually intercepting a penetration through the concrete with outlet to the atmosphere. The outlet is postulated to arise from concrete penetrations from piping and airlocks and inadequate concrete bonding. Other alternative pathways are possible. For example, gas could flow through the concrete, if the concrete permeability is relatively high, or gas could also escape through cracks in the concrete. These alternative pathways were not considered in the present analysis. These may need to be revisited in future follow-up work to evaluate the extent of leakage through those alternative pathways compared to the gap pathway considered in this report.

Al-Hussainy, et al. (1966) provide the continuity equations to describe flow of gases through porous media, such as the corrosion product build up in the corrosion damaged zone of the

liner. The mass flux as a function of the pressure, in the laminar flow regime is given by Darcy's law

$$J = \rho v = -\frac{P}{R T} \frac{\kappa}{\mu} \nabla P = -\frac{\kappa P}{\mu} \nabla \frac{P}{R T} = -\frac{\kappa P}{\mu} \nabla \rho \quad [3-10]$$

κ is the permeability and μ is the viscosity of vapor, and the system is assumed isothermal. The continuity equation is

$$\nabla \cdot \left(\frac{\kappa P}{\mu} \nabla \rho \right) = \theta \frac{\partial \rho}{\partial t} \quad [3-11]$$

where θ is the system porosity. This equation is similar to a diffusion equation, with a pneumatic diffusivity that is pressure dependent

$$D_e = \frac{\kappa P}{\mu \theta} = \frac{a^2 P}{12 \mu \theta} \quad [3-12]$$

Table F-61 of the CRC Handbook of Chemistry and Physics (Weast and Astle, 1981) provides information to define the viscosity as a function of the temperature. The permeability, κ , for Poiseuille flow between flat plates is related to the aperture a (i.e., the spacing between the liner and the concrete) as $\kappa=a^2/12$ (Witherspoon, et al., 1980; Bird, et al., 1960). For the free space between the liner and the concrete, $\theta=1$. The initial pressure is assumed to be the atmospheric pressure: $P(x,t=0)=P_{atm}$, and the initial temperature is the initial temperature of the input transient. The boundary conditions are

$$\rho(x = 0; t) = \rho_A(t) = \frac{m_A(t)}{V} = \frac{P_A(t)}{R T_A(t)} \quad [3-13]$$

and

$$\rho(x = L; t) = \frac{P_{atm}}{R T_A(t)} \quad [3-14]$$

The geometrical abstraction of the system is depicted in Figure 3-4. From Figure 3-4(b), the equivalent cross section of the inlet is defined as a harmonic average

$$A_{eq} = \frac{1}{\frac{1}{\pi r^2 \theta} + \frac{1}{2 \pi r a}} \quad [3-15]$$

The factor θ is a porosity or screen factor to account for resistance of corrosion products to gas flow; r is the equivalent radius of the corrosion patch, and a is the aperture. In Eq. [3-15] it is implicitly assumed that the permeability of the corrosion product is relatively high. The only effect of the presence of the corrosion product is a decrease in the effective area for flow. This approximation of high permeability merits some experimental verification: it may be possible for corrosion products to be relatively impermeable and, thus, offer significant resistance to flow.

From Figure 3-4 (c), the equivalent cross section of the outlet is the surface of a ring of radius r_o

$$A_o = 2 \pi r_o a \quad [3-16]$$

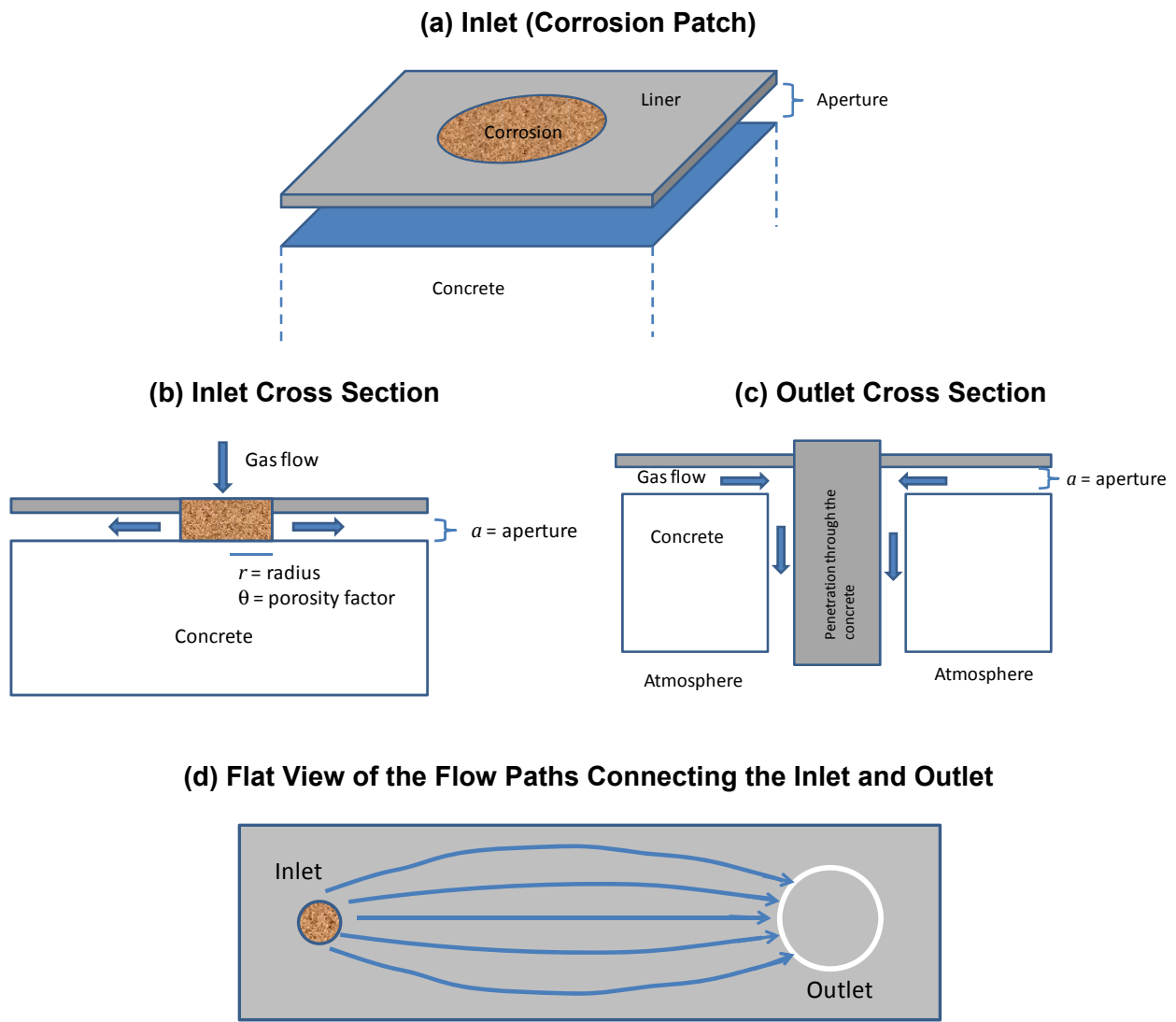


Figure 3-4. Geometrical Abstraction of the Flow Pathway. (a) Pathway Inlet (Corrosion Patch), (b) Inlet Cross Section, (c) Outlet Cross Section, and (d) 2-Dimensional View of the Pathway

The width of the pathway [vertical direction in Figure 3-4(d)] is represented with the symbol W , and the length [horizontal direction in Figure 3-4 (d)] with L .

The rate of mass transfer from A to B, r_{AB} , is

$$r_{AB} = -\frac{a^2 P_A}{12 \mu(T_A)} A_{eq} n \cdot \nabla \rho|_{x=0} = -\frac{P_A}{R T_A} \frac{a^2}{12 \mu(T_A)} A_{eq} n \cdot \nabla P|_{x=0} \quad [3-17]$$

The vector n is a unit normal vector, depicted in Figure 3-5. The rate of mass transfer from B to the atmosphere, $r_{B,atm}$, is

$$r_{B,atm} = -\frac{a^3 \pi r_o P_{atm}}{6 \mu(T_A)} n \cdot \nabla \rho|_{x=L} = -\frac{P_{atm}}{R T_A} \frac{a^3 \pi r_o}{6 \mu(T_A)} n \cdot \nabla P|_{x=L} \quad [3-18]$$

The radius of the penetration through the concrete is r_o and L is the length of the pathway. Equations [3-17] and [3-18] are consistent with cubic laws for mass flow through cracks. This proportionality to a^3 is a dominant dependence controlling gas release rates, as discussed later.

If the pressure of A drops below B (for example due to the action of the ECCS), then $r_{AB}=0$, and the rate of mass transfer from B to A, r_{BA} , is

$$r_{BA} = \frac{P_A}{R T_A} \frac{a^2}{12 \mu(T_A)} A_{eq} \frac{\partial P}{\partial x}|_{x=0} \quad [3-19]$$

The system of mass and energy balance equations were numerically solved using the GoldSim software (GoldSim Technology Group, LLC., 2013), as well as the gas diffusion equation, Eq. [3-1]. The 2-dimensional grid in Figure 3-5 is a pathway footprint (footprint of the liner-concrete gap space through which gas is postulated to flow). The inlet (corrosion area) and outlet (penetration to the atmosphere) were only connected to the central element in the grid. Additional discretization was applied to connect the inlet to the pathway, and the pathway to the outlet (additional discretization not shown in Figure 3-5), to correct for the fact that the inlet and outlet holes are in general much smaller than pathway mesh elements in Figure 3-5. No flow boundary conditions were applied at the edges of the domain (i.e., all gas is assumed to remain inside the domain). The pneumatic diffusivity during a timestep was approximated using the gas density, pressure, and temperature from the previous timestep, for example

$$D_e^i = \frac{a^2 P^{i-1}}{12 \mu(T_A^{i-1})} = \frac{a^2 R \rho^{i-1} T_A^{i-1}}{12 \mu(T_A^{i-1})} \quad [3-20]$$

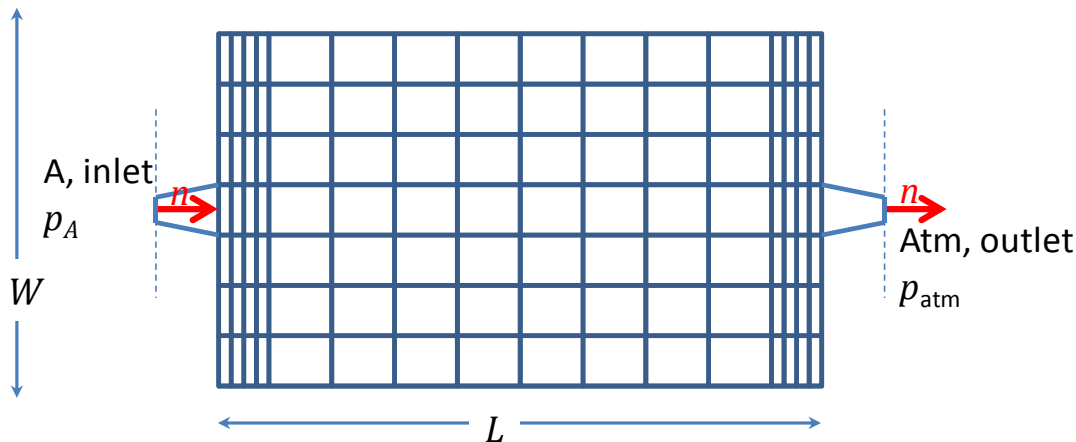


Figure 3-5. Grid Structure Used to Numerically Solve the Gas Flow Equation

Densities, ρ^{i-1} , vary from grid position to grid position. A more precise solution can be implemented using differential equation solvers such as COMSOL. Note, however, the boundary conditions in Eq. [3-13] and [3-14] include feedback: if a significant amount of gas is released, the pressure and temperature, P_A and T_A , are lowered, which in turn affect the rate of transport through the B pathway. If the leak rate is small, then P_A and T_A , are almost independent of the gas leaked, and the functions $P_A(t)$ and $T_A(t)$ can be directly input to a differential equation solver. A 3-dimensional differential equation solver can account for the cylindrical geometry of the containment building, circumferential flow, and variable aperture. Nonetheless, the simplified model implemented in GoldSim captures the main physics and couplings of the problem, and has flexibility to yield insights on factors controlling leakage to the atmosphere. Results of the computations are summarized in the next section.

In the present analysis it is assumed that the concrete is impermeable, to ignore gas flow through the concrete. The Eq. [3-12] can be used to establish when such assumption is reasonable. For a back-of-the-envelope computation, consider a system with a vapor temperature of 420 K [296 °F] and pressure of 5 atm [73 psi]. The viscosity of vapor, for those conditions, is approximately 1.4×10^{-4} g/(cm-s) (Weast and Astle, 1981). If $L_c=1.2$ m is the thickness of the concrete wall, the time it would take for gas to flow through the concrete, t_L , can be estimated as L_c^2/D_e , or, substituting using Eq. [3-12]

$$t_L = 4.7 \times 10^{-16} d m^2 \frac{\theta}{\kappa} \quad [3-21]$$

Reasonable values of the concrete permeability and porosity are $\kappa=10^{-17}$ m² and $\theta=0.2$; which values would yield an approximate penetration time on the order of 9 days. This estimate is clearly conservative, as the pressure and temperature will decrease with time due to the action of the emergency core cooling system. For example, under a constant pressure of 1 atm [14.7 psi], the penetration time would be on the order of 50 days. If the permeability is one order of magnitude higher, the penetration time would be on the order of one day, at a constant temperature and pressure of 420 K [296 °F] and 5 atm [73 psi]. Therefore, if the concrete permeability is less than 10^{-17} m², the assumption of impermeable concrete is reasonable. However, permeability values on the order of 10^{-17} m² or higher appear possible (e.g., Pabalan et al., 2009), in which case leakage through the concrete could importantly contribute to the total leak rates. Note, however, that other processes such as condensation within the concrete would also increase flow resistance and decrease leak rates.

3.4 Comparison to Leak Tests

Integrated leak tests (type A leak rate test) were performed on North Anna Unit 2 following discovery of the 0.635-cm [0.25-in] diameter through-wall hole on the liner, up to a design peak accident pressure of 59.7 psia [4 atm]. The measured leak rate was approximately 0.007 percent/day (Beaver Valley Power Station, 2009). The allowable containment leak rate is 0.1 percent/day.

A pressure ramp, with a linear increase of 1 to 4.95 atm [14.7 to 72.8 psi] in 10 hours, was input to the leak model, to compare to North Anna Unit 2 leak tests. The pressure as a function of time and position (position measured along the centerline in Figure 3-5) is displayed in Figure 3-6. The length L was assumed to be 5 m [16 ft], and the aperture, $a=0.04$ mm [1.57 mil].

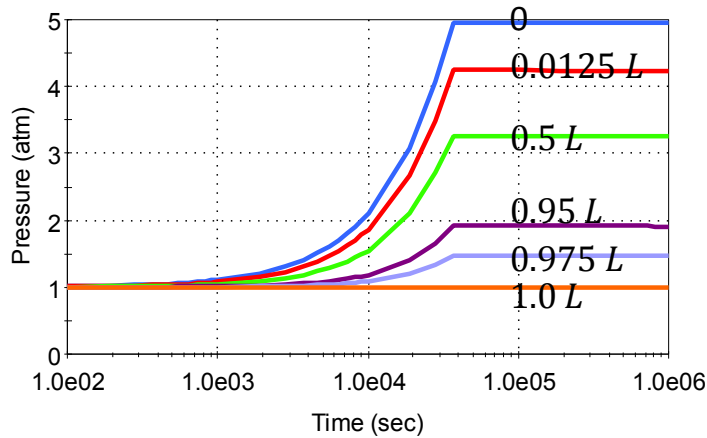


Figure 3-6. Pressure As a Function of Time and Position With a Position Measured Along the Centerline of Figure 3-5

Figure 3-7 includes plots of the fractional release and cumulative release to the atmosphere as functions of time and the aperture, a . The aperture is shown to be the most important feature controlling gas release to the atmosphere. From values of the fractional release at the end of

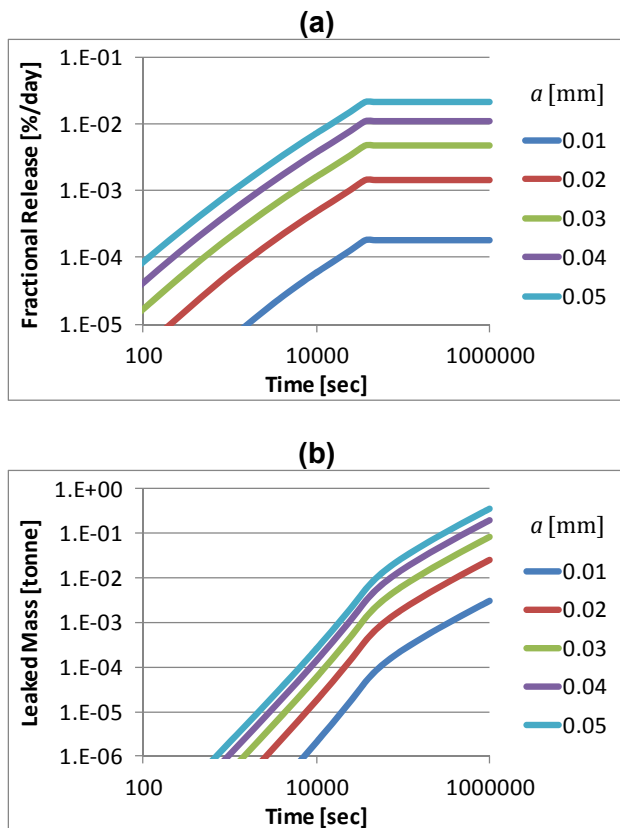


Figure 3-7. (a) Fractional Release and (b) Cumulative Leak as Functions of Time and the Aperture, a . Values of the Aperture Are Indicated in the Plots in Units of mm.

the simulation time in

Figure 3-7(a), results similar to the North Anna Unit 2 leak tests are obtained if the effective aperture is between 0.03 and 0.04 mm [1.18 and 1.57 mil]. To further investigate the effect of physical parameters on the leak rate, simulations varying one-parameter-at-a-time were performed, and the results are presented in Figure 3-8. Central values used in the simulations are listed in Table 3-2.

Figure 3-8(d)–(e) shows variation of the fractional release as a function of the length, L , and width, W . The fractional release decreases with increasing L due to the establishment of less steep pressure gradients. Since the release rate to the atmosphere is proportional to the local pressure gradient, longer travel distances imply lower rates of release. On the other hand, the fractional release tends to increase with increasing W . This is because the release is directly related to the pathway cross section: $W \times a$. However, as the pathway widens, gas travels a longer distance to intersect the outlet, which tends to lower the release. Because of this competition, the fractional release increases with W , but in a less than linear manner. Given the range of variability in the fractional release as a function of the length and width, it is concluded that L and W are not critical factors to constrain the release rate and fractional release.

Finally, Figure 3-8(f) and (g) show the variation of the fractional release with the pathway aperture. The logarithmic scale plot in Figure 3-8(f) displays more than two orders of magnitude variation by changing a from 0.02 to 0.13. A polynomial fit to the linear-scale curve in Figure 3-8(g) indicates that the fractional release is proportional to a^3 . The pathway aperture, a , is the critical parameter controlling the release rate, under the assumption of impermeable concrete.

3.5 Sensitivity Analyses

Sensitivity analyses were performed to quantify the effect of uncertainty in model parameters on the leak rate, considering fixed values of the pathway aperture. The considered input transients are the PWR containment transients in the ASTM D 3911 standard (ASTM International, 2003). A Monte Carlo approach was selected to propagate the uncertainty. In the Monte Carlo realizations, parameters such as pathway length, width, corrosion area, and θ were sampled to account for uncertainty. The synthesis model in Chapter 2 was used to compute the corrosion area as a function of the ionic concrete resistivity and the other uncertain parameters of the

corrosion model discussed in Chapter 2. The input parameters and distributions are summarized in Table 3-3. Results of the Monte Carlo runs are summarized in the following figures.

Figure 3-9 shows ranges of fractional release as function of the aperture. Figure 3-9(a)–(d) display confidence intervals of the fractional release rate as a function of time for different values of the aperture. If the aperture is less than 0.01 mm [0.4 mil], the system is tight and release is negligible (under the assumption of impermeable concrete). Releases comparable to the allowable containment leak rate of 0.1 percent/day were computed with $a=0.1$ mm [3.9 mil]. Releases well in excess to the allowable leak rate were computed with $a=0.5$ mm [19.7 mil]. If the aperture is 1 mm or more, the system is practically open, offering minor resistance to leakage. Figure 3-9(e) shows a comparison of means of fractional releases as function of time, associated with different apertures. Figure 3-9(f) is a plot of the maximum fractional release,

from Figure 3-9(e), versus the aperture. Similarly as in Figure 3-8(g), the fractional release is approximately proportional to a^3 .

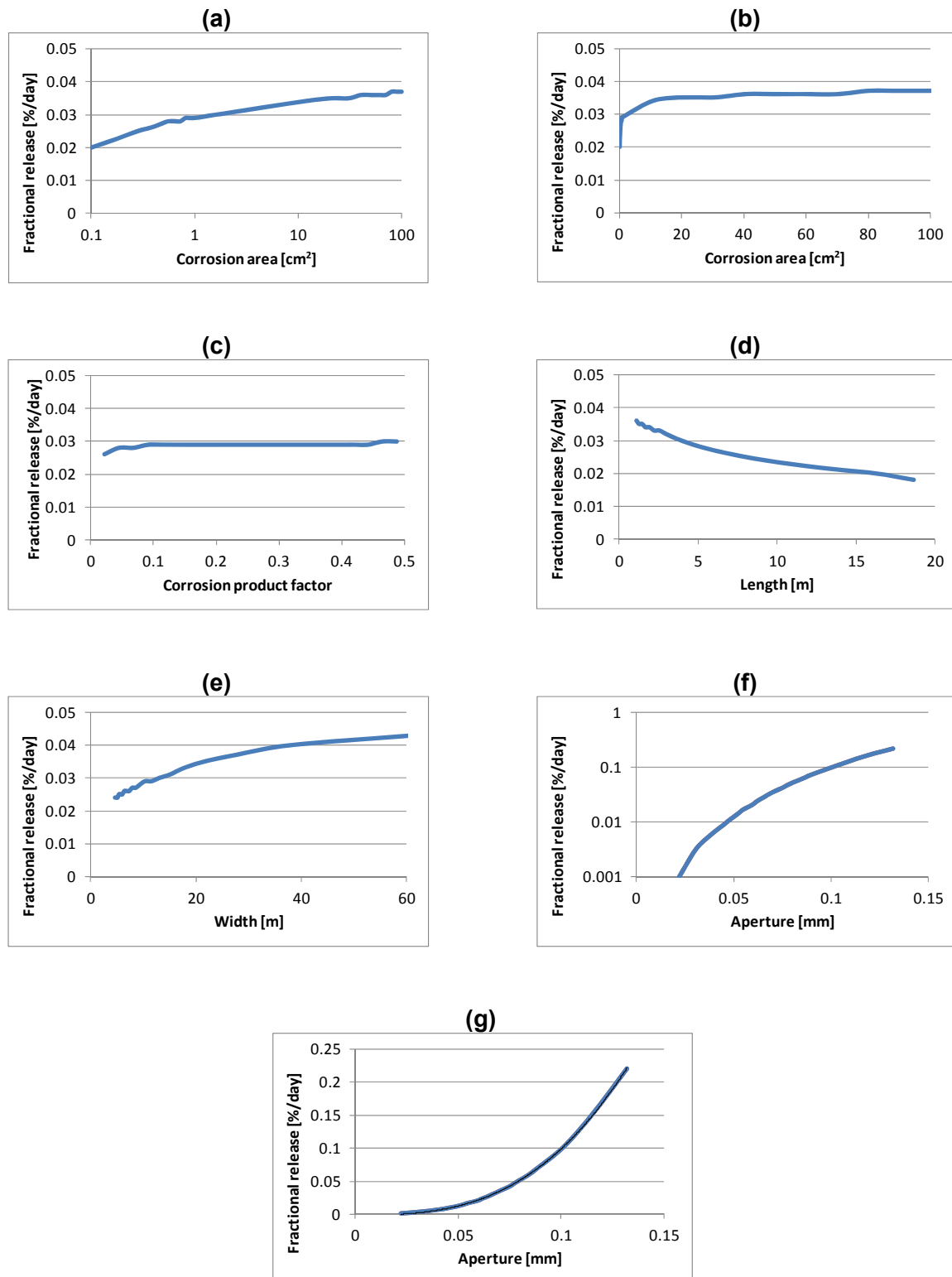


Figure 3-8. Fractional Release As a Function of Model Parameters.

**Only One Parameter Was Varied, While the Others Were Held Constant.
The Vertical Axis Is the Leak Rate at 10^6 Seconds.**

Table 3-2. Central Values of Models Parameters Used for Results in Figure 3-7.

Only the Value of One Parameter Was Varied in Each Plot in Figure 3-7.

Parameter	Central Value	Parameter	Central Value
a	0.04 mm	θ	0.05
L	5 m	Area (corrosion)	1 cm ²
W	20 m	r_o	10 cm

Table 3-3. Distributions and Values of Model Parameters for Monte Carlo Leak Rate Computations

Parameter	Description and Unit	Distribution or Value
Parameters of the corrosion model to estimate a corrosion area		
p	Ionic concrete resistivity [k Ω -cm]	Triangular [10, 20, 50]
c	Ohmic resistance constant (see Eq. [2-1])	Uniform[4, 4.8]
i_{pass}	Passive current density of the carbon steel [μ A/cm ²]	0.01
$i_{O_2}^o$	Normalized exchange current density for oxygen reduction [μ A/cm ²]	Triangular[0.0045, 0.015, 0.026]
pH	pH of the anode [-]	Triangular [4, 6, 7]
Parameters of the leak rate model		
θ	Corrosion product porosity factor [-]	Uniform[0.01, 0.5]
a	Pathway aperture [mm]	Triangular[0.01, 0.05, 0.15]
L	Pathway length [m]	Log-uniform[1, 20]
L/W	Length to width ratio [-] (This parameter is assumed correlated to L , with 0.7 as correlation coefficient. This correlation is used to avoid unphysical pathway widths.)	Uniform[1/20, 1]
r_o	Radius of penetration defining the pathway outlet [cm]	10

Figure 3-10 presents two examples of the average pressure as a function of time and position along the diffusive pathway in Compartment B. The position is indicated in labels in Figure 3-10 as a fraction of the pathway length, L , measured along the centerline of Figure 3-5. Figure 3-10(a) and (b) are average pressures (from 500 Monte Carlo realizations) computed using $a=0.01$ mm [3.9 mil] and $a=0.5$ mm [19.7 mil], respectively. The curves for the average pressure versus time are similar because the flow domain is bounded. Early pressures in Figure 3-10(a) are smaller than in Figure 3-10(b) because the pneumatic diffusivity is smaller in the former case, and, thus, it takes longer for the pressure front to travel through the pathway.

Figure 3-11 shows fractional release versus time including variation in the pathway aperture. Figure 3-11(a) presents confidence intervals on the fractional release rate. Figure 3-11(b) and (c) are scatter plots of the maximum (in time) of the fractional release versus the pathway aperture. The maximum fractional release is proportional to a^3 , as in previous cases. The plots in Figure 3-11(b) and (c) include a dashed line with the allowable containment leak rate. It is inferred that if the effective aperture is less than 0.08 mm [3.1 mil], the fractional release is unlikely to exceed the allowable leak rate, independent of other factors such as the area of the corrosion damage, and the length and width of the pathway (under the assumption of impermeable concrete). The realizations with large fractional release, above the allowable leak

rate, correspond to realizations with large aperture, small pathway length, L , and large area of corrosion damage. The dominant trend in Figure 3-11 (b) and (c) is proportional to a^3 . Scatter around the dominant trend is the result of the variation of secondary parameters (e.g., corrosion area, θ , L , W).

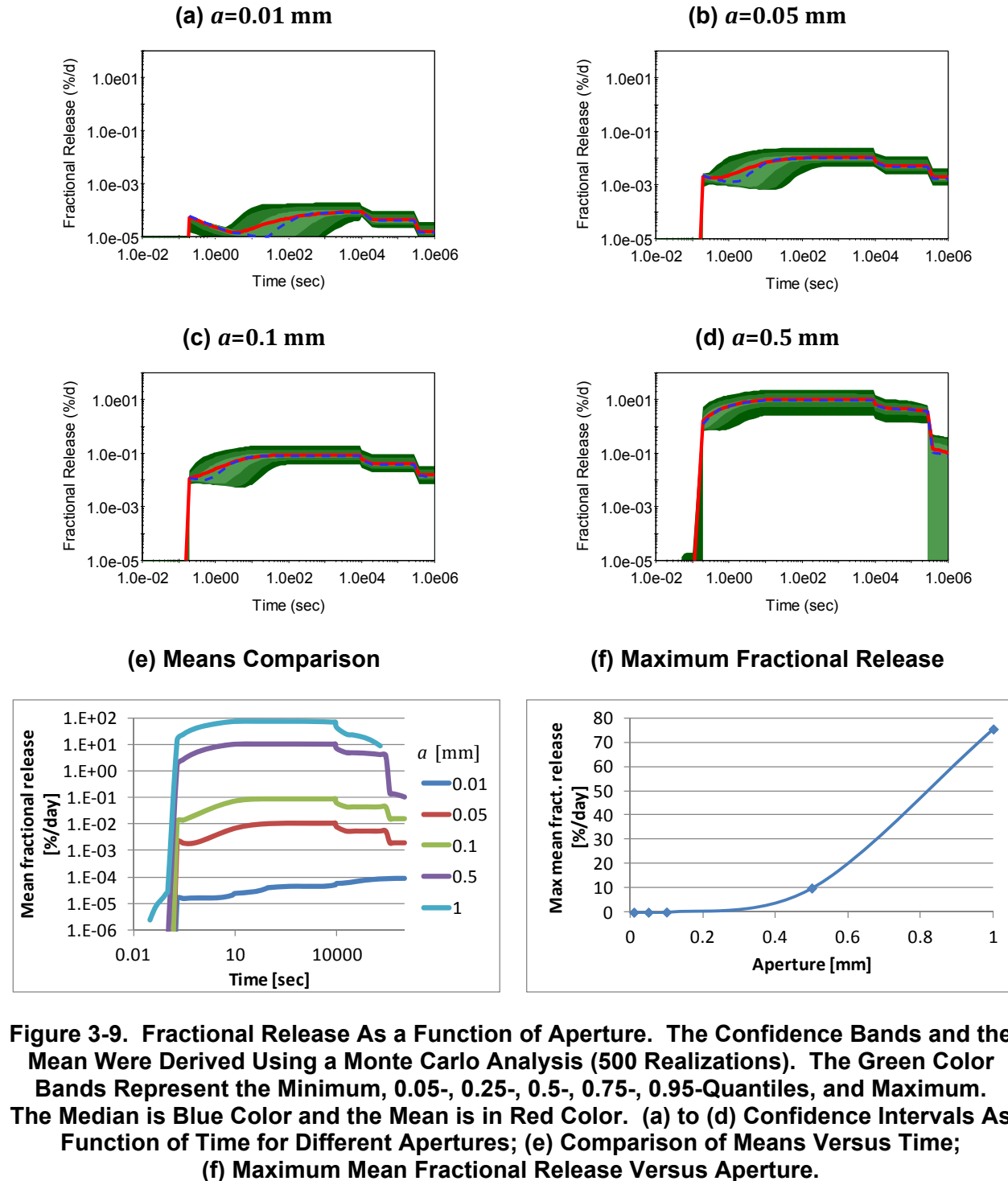
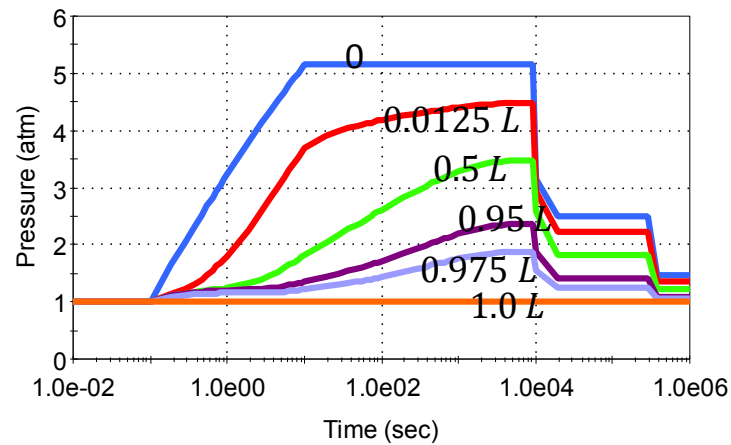


Figure 3-9. Fractional Release As a Function of Aperture. The Confidence Bands and the Mean Were Derived Using a Monte Carlo Analysis (500 Realizations). The Green Color Bands Represent the Minimum, 0.05-, 0.25-, 0.5-, 0.75-, 0.95-Quantiles, and Maximum. The Median is Blue Color and the Mean is in Red Color. (a) to (d) Confidence Intervals As Function of Time for Different Apertures; (e) Comparison of Means Versus Time; (f) Maximum Mean Fractional Release Versus Aperture.

(a) $a=0.01$ mm



(b) $a=0.5$ mm

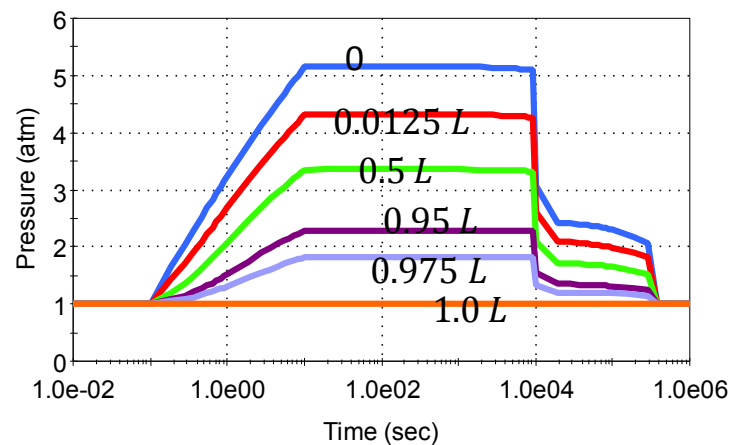


Figure 3-10. Average Pressure (From 500 Monte Carlo Realizations) As a Function of Time and Position, With a Position Measured Along the Centerline of Figure 3-5, for Two Apertures. The Position Is Indicated With Labels in the Figure in Units of L .

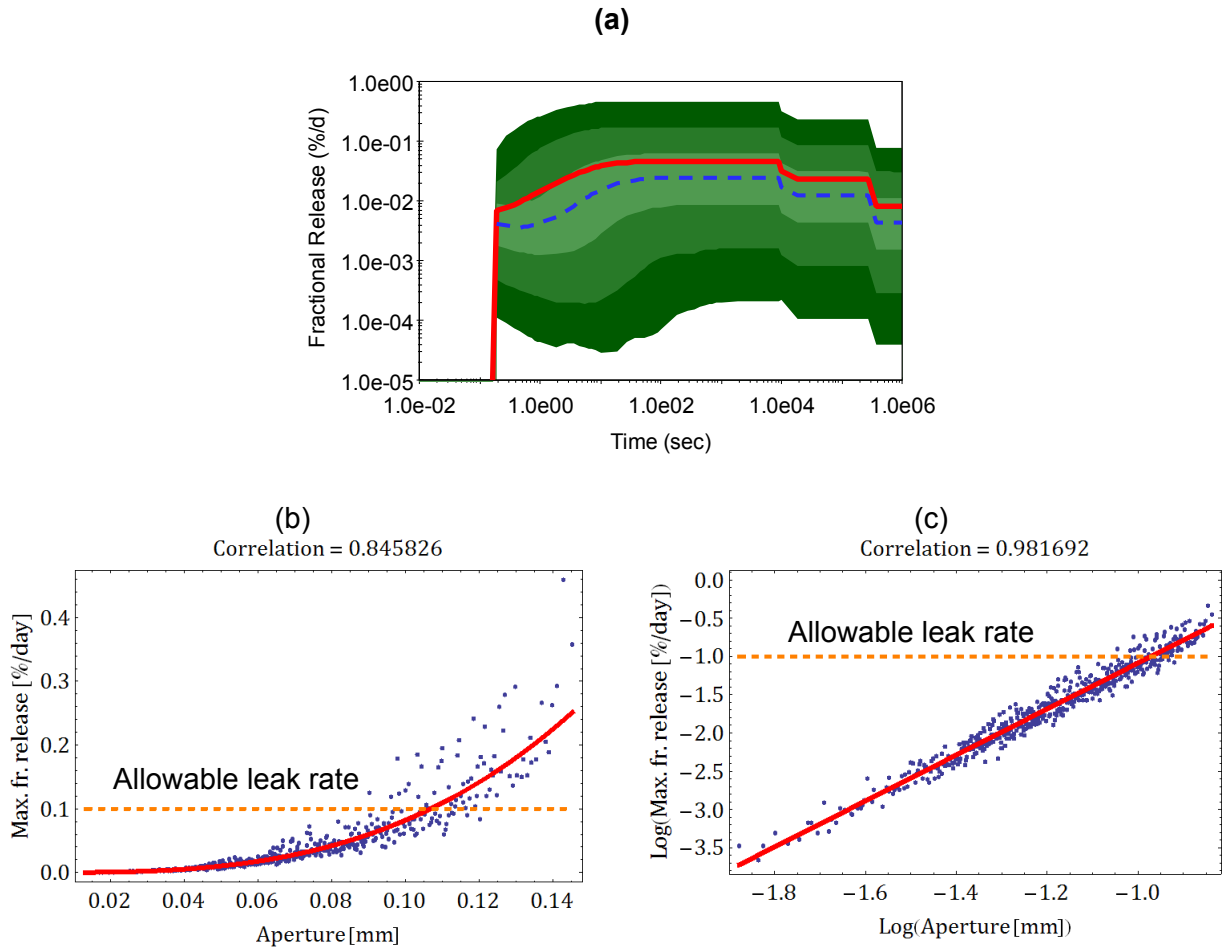


Figure 3-11. Sensitivity Analysis on the Fractional Release Including Variation in the Aperture. (a) Confidence Intervals on the Fractional Release As a Function of Time; (b) Scatter Plot of the Maximum of the Fractional Release Versus Aperture; and (c) Same As (b) With a Log-10 Transformation. The Red Line Is a Curve Proportional to the Cube of the Aperture.

The effective aperture, a , is an integrated, effective, property of the pathway. In reality, the pathway will be heterogeneous, with varying aperture. Near the corrosion damage, due to the nature of the corrosion process, the aperture at the inlet is expected to be tight. Corrosion requires the establishment of an acidic environment, which can only be sustained if wood is in close contact with the liner. Macrocell corrosion requires clear differentiation between the porewater chemistry at the anode and cathode, which can be also be sustained if the contact is tight. In addition, corrosion products expand, closing gaps. Therefore, the aperture at the inlet is likely to be small. The gap or aperture may be wider in other regions of the pathway.

Care must be exercised not to interpret a as the tightest gap between the liner and the concrete, as such a region may not be accessible to gas flow (i.e., it would not be part of the pathway).

Gas will flow along the path of least resistance, and move around tight gaps, if wider gaps are accessible. Very likely the effective average aperture is determined by the liner-concrete contact near the inlet.

Based on the calibration to leak tests in North Anna Unit 2, it is concluded that a reasonable pathway aperture is on the order of 0.1 mm or less, under the assumption of impermeable concrete. The size of the through-wall corrosion area is unlikely to control the leak rate, except when the corrosion area is small.

3.6 Discussion—Leak Rate Model

A mass and energy balance model was developed to estimate the pressure, temperature, and mass of vapor in the containment building, considering temperature and pressure transients in the ASTM D3911-03 standard for PWR containment for post LOCA conditions. These stylized transients bound transients typically considered in Updated Final Safety Analysis Reports as part of analyses of containment response to LOCAs. Ideal gas equations were used to compute mass, density, pressures, and temperatures, assuming an adiabatic system. The mass balance model was coupled to a 2-dimensional gas flow model to compute gas transport through the leak pathway. The leak pathway is postulated to be a narrow space (space between the liner and concrete) until an outlet to the atmosphere is intercepted. The outlet to the atmosphere is postulated to arise from an existing penetration through the concrete, such as those from piping or airlocks and inadequately sealed concrete. Other potential pathways such as through-wall concrete cracks or flow through porous concrete were not considered in the analysis. The gas flow model is used to compute the gas leak rate to the atmosphere, which in turn provides feedback to the mass balance model to compute the amount of vapor remaining in the containment building, its pressure, and its temperature.

Beaver Valley Power Station performed estimates of leak rates through a small corrosion hole on the liner, based on integrated air leak tests from North Anna Unit 2 (Beaver Valley Power Station, 2009). Those integrated air leaks tests that were considered in the present analysis to calibrate the model to estimate parameters such as the aperture of the narrow space between the liner and the concrete. Sensitivity analyses were performed to understand contributions from uncertain parameters to the leak rate. The most important parameter controlling leak rates is the pathway aperture (i.e., the gap between the liner and the concrete), under the implicit assumption of impermeable concrete (see the end of Section 3.3 for a brief discussion on the validity of this assumption). Leak rates were found to be proportional to the cube of the pathway aperture. Based on calibration to leak tests in North Anna Unit 2, it is concluded that a reasonable pathway aperture is on the order of 0.1 mm [3.9 mil] or less. The size of the through-wall corrosion area is unlikely to control the leak rate, except when the corrosion area is small, less than 1 cm² [0.16 in²].

The effective aperture, a , is a representative aperture that depends on the variation in the local apertures throughout the pathway. The physical pathway will be heterogeneous. Near the corrosion damage, due to the nature of the corrosion process, the aperture at the inlet is expected to be tight. Corrosion requires the establishment of an acidic environment, which can only be sustained if the wood is in close contact with the liner. In addition, corrosion products expand, closing gaps. Therefore, the aperture at the inlet is likely to be small. Sensitivity analyses were used to argue that order of magnitude estimates in the length and width are sufficient to derive reasonable estimates of leak rates, and that the area of the corrosion damage on the liner is not necessarily a factor controlling leak rates

The following bullets summarize main conclusions of the analysis, assumptions and limitations of the analysis, and potential additional studies to reduce uncertainties.

Main Conclusions of the Analysis

- Under the assumption of impermeable concrete, an aperture on the order of 0.1 mm [3.9 mil] or less can be used to compute fractional leak rates comparable to North Anna Unit 2 integrated leak tests
- The pathway aperture is the dominant factor controlling release rates
- Fractional leak rates are likely to be below the allowable containment leak rate of 0.1 percent per day if the effective aperture is less than 0.08 mm [3.1 mil]
- Leak rates are controlled by the area of the liner corrosion damage, if this area is less than 1 cm² [0.16 in²]; for larger areas, the leak rate is controlled by the pathway aperture

Analysis Assumptions and Limitations

- Through-wall cracks in the concrete were not considered
- Gas flow through the concrete was ignored (this is equivalent to assuming the concrete is impermeable). See the end of Section 3.3 for back-of-the-envelope computations on when this assumption may be reasonable.
- Corrosion products were assumed to be highly permeable (i.e., corrosion products are assumed to offer minimal resistance against gas flowing through the liner corroded area)
- Flow through the leakage pathway is laminar (i.e., turbulent flow is disregarded)
- Heterogeneity in the pathways is not considered (e.g., retaining studs connecting the liner to the concrete are not considered, the gap distance between the liner and the concrete is expected to be variable)
- The pathway is a simple rectangular pathway (e.g., wrap-around flow arising in a cylindrical geometry is not considered)
- Effects of post LOCA pressures, such as compressing of corrosion products at the through-wall corroded site and pressing of the liner into the concrete, are not considered

Potential Additional Studies to Reduce Uncertainties

- Measure the permeability of representative corrosion products
- Determine the permeability of concrete
- In leak tests, record transients (i.e., pressure versus time) to provide more additional information to calibrate leak models

- Develop leak models accounting for (i) heterogeneity in the leak pathway (e.g., variable aperture, presence of retaining studs attaching the liner to the concrete), (ii) flow through the concrete, (iii) corrections to account for potential turbulent flow, (iv) flow condensation, and (v) 3-dimensional pathway geometries (e.g., cylindrical pathway)

4 CONCLUSIONS

The main points concluded in the report are summarized in the following bullets:

Corrosion Model

- Macrocell corrosion is a feasible process explaining the observed instances of liner through-wall corrosion.
- Computed corrosion rates considering concrete porewater with pH lowered by acetic acid (an organic acid that forms by wood degradation) are consistent with corrosion rates inferred from observed instances of through-wall corrosion.
- The concrete ionic resistivity is an important parameter controlling corrosion rates and the extent of damage.
- If concrete ionic resistivity is on the order of 10 kΩ-cm, other physical parameters (oxygen diffusion through concrete, kinetic rates of oxygen reduction and iron passive dissolution, and the amount of rebar embedded in the concrete) play a secondary role to determine the extent of damage.
- Static corrosion areas ranging from a few to a few tens of square centimeters are predicted by the corrosion model, under defined assumptions (e.g., resistivity ranging from 10 to 50 kΩ-cm, driving potential on the order of 600 mV, pH at the anode ranging from 4 to 7, ignoring the dimensions of the liner-wood contact area), but the upper bound is likely limited in reality by the dimensions of the contact area.

Leak Rate Model

- The gap distance between the liner and the concrete (referred to aperture) is the most important parameter controlling leak rates, under the implicit assumption of impermeable concrete.
- Other parameters of the leak rate model (length and width of the pathway, area of the liner corrosion damage) play a secondary role on determining leak rates.
- The area of the corrosion damage on the liner controls leak rates when the area is small (e.g., smaller than 1 cm² [0.16 in²]). When the area is large, leak rates are controlled by the aperture.
- Leak rates are mostly proportional to the cube of the aperture.
- Computations considering pathways with effective apertures less than 0.1 mm [3.9 mil] produce leak rates consistent with an integrated leak test at North Anna Unit 2. If the aperture is less than 0.01 mm [0.39 mil], computed leak rates are negligible, well below the allowable containment leak rate of 0.1 percent/day.
- The aperture at the pathway entry is expected to be small, because macrocell corrosion requires a tight contact between the liner and the wood, and corrosion products expand in volume.

The conclusions are conditional on assumptions and limitations of the model, which are summarized in the next bullets. A more detailed corrosion model is expected to result in lower corrosion rates and slower rates for lateral growth along the liner surface. Some leak pathways were ignored (e.g., gas flow through the concrete), which consideration could increase the leak rate estimates.

Main Limitations and Assumptions of the Analyses

- The corrosion model is steady-state. Accordingly, the rate of corrosion propagation is ignored, as well as other time dependencies such as variation in the porewater chemistry near the anode, corrosion product buildup and feedback on corrosion rates.
- The corrosion model disregards constraints imposed by limited contact area between the foreign wood and the liner.
- Estimates on the extent of the area of the corrosion damage on the liner are strongly dependent on assumed values of the concrete ionic resistivity and predictions of the corrosion rate as a function of pH and the driving potential.
- In the leak model, alternative pathways such as through-wall cracks in the concrete and gas flow through the concrete were ignored (this is equivalent to assuming the concrete is impermeable).
- Corrosion products were assumed to be highly permeable.

5 REFERENCES

- Al-Hussiny, R., H.J. Ramey, and P.B. Crawford. "The Flow of Real Gases Through Porous Media." *Journal of Petroleum Technology*. May Issue. pp. 624–636. 1966.
- Anderko, A. "Modeling of Aqueous Corrosion." *Shreir's Corrosion*. 4th Edition. Vol. 2. Amsterdam, The Netherlands: Elsevier. pp. 1,585–1,629. 2010.
- Anderko, A., P. McKenzie, and R.D. Young. "Computation of Rates of General Corrosion Using Electrochemical and Thermodynamic Models." *CORROSION*. Vol. 57, No. 3. pp. 202–213. 2001.
- Andersson, K., B. Allard, M. Bengtsson, and B. Magnusson. "Chemical Composition of Cement Pore Solutions." *Cement and Concrete Research*. Vol 19. pp. 327–332. 1989.
- ASME. "ASME Boiler and Pressure Vessel Code." New York, NY: ASME. 2008.
- ASTM International. D 3911 – 03, "Standard Test Method for Evaluating Coatings Used in Light-Water Nuclear Power Plants at Simulated Design Basis Accident (DBA) Conditions." West Conshohocken, PA: ASTM International. 2003.
- Beaver Valley Power Station, Unit No. 1. "Licensee Event Report (LER) 2009-003-00, Containment Liner Through Wall Defect Due to Corrosion." Letter from Peter P. Sena III to the U.S. Nuclear Regulatory Commission, dated June 18, 2009. Docket Number 05000334, LER 2009-003-00. ADAMS Accession Number ML091740056. Shippingport, PA: Beaver Valley Power Station. 2009.
- Bertolini, L., B. Elsener, P. Pedefterri, and R. Polder. "Corrosion of Steel in Concrete—Prevention, Diagnosis, Repair." DOI: 10.1002/3527603379. Weinheim, Germany: WILEY-VCH Verlag GmbH & Co. KGaA. 2004.
- Bird, R.B., W.E. Stewart, and E.N. Lightfoot. *Transport Phenomena*. New York City, New York: John Wiley & Sons. 1960.
- COMSOL, Inc. "COMSOL Multiphysics®." Burlington, Massachusetts: COMSOL, Inc. 2013. <<http://www.comsol.com/>> (March 8, 2013).
- Constantiner, D. and S. Diamond. "Pore Solution Analysis: Are There Pressure Effects?" *Mechanisms of Chemical Degradation of Cement-Based Systems*. K.L. Scrivener and J.F. Young, eds. London, United Kingdom: E&FN Spon. 1997.
- Dunn, D.S, A.L. Pulvirenti, and M.A. Hiser. "Containment Liner Corrosion Operating Experience Summary: Technical Letter Report—Revision 1." ADAMS Accession Number ML112070867. Washington, DC: U.S. Nuclear Regulatory Commission. 2011.
- Gaskell, D.R. *Introduction to the Thermodynamics of Materials*. 3rd Edition. Washington, DC: Taylor & Francis. 1995.

Gerbino, A. "A Guide for Using the OLIAnalyzers." Morris Plains, New Jersey: OLISystems, Inc. 2006. <<http://support.olisystems.com/Documents/Manuals/TricksOfTheTrade.pdf>> (March 5, 2013).

GoldSim Technology Group, LLC. "GoldSim Version 10.5." Issaquah, Washington: GoldSim Technology Group, LLC. 2013. <<http://www.goldsim.com/Home/>> (March 11, 2013).

Gulikers, J. "Numerical Modeling of Reinforced Corrosion in Concrete." *Corrosion in Reinforced Concrete Structures*. H. Böhni, ed. Boca Raton, Florida: CRC Press, LLC. 2005.

Hendrix, D.E. "Current Status Regarding the Corrosion of Metals in Contact With Preservative-Treated Wood." Report WOW-5056. Atlanta, Georgia: Arch Wood Protection. 2006.

Huet, B., V. L'hostis, G. Santarini, D. Feron and H. Idrissi. "Steel Corrosion in Concrete: Determinist Modeling of Cathodic Reaction As a Function of Water Saturation Degree." *Corrosion Science*. Vol. 49. pp. 1,918–1,932. 2007.

Kranc, S.C. and A.A. Sagüés. "Detailed Modeling of Corrosion Macrocells on Steel Reinforcing in Concrete." *Corrosion Science*. Vol. 43. pp. 1,355–1,372. 2001.

Kranc, S.C. and A.A. Sagüés. "Computation of Reinforcing Steel Corrosion Distribution in Concrete Marine Bridge Substructures." *CORROSION*. Vol. 50. pp. 50–61. 1994.

Li, X. "Mitigating Alkali Silica Reaction in Recycled Concrete." Ph.D. Thesis. Durham, New Hampshire: University of New Hampshire. 126 pp. 2005.

Los Alamos National Laboratory. NUREG/CR-6914, "Integrated Chemical Effects Test Project: Consolidated Data Report." Washington, DC: U.S. Nuclear Regulatory Commission. 2006.

Moran, M.J. and H.W. Shapiro. *Fundamentals of Engineering Thermodynamics*. 4th Edition. New York: John Wiley & Sons, Inc. 2000.

Neville, A.M. *Properties of Concrete*. 4TH Edition. London, United Kingdom: John Wiley & Sons. pp. 346–350. 1996.

Newman, J. "Resistance for Flow of Current to a Disk." *Journal of the Electrochemical Society*. Vol. 113, Issue 5. pp. 501–502. 1966.

NRC. NUREG-1037, "Containment Performance Working Group Report." Washington, DC: U.S. Nuclear Regulatory Commission. 1985.

OLISystems, Inc. "OLIAnalyzer Studio." Morris Plains, New Jersey: OLISystems, Inc. 2013. <<http://www.olisystems.com/new-streamanalyzer.shtml>> (March 18, 2013).

Ozbolt, J. G. Balabanic, and M. Kuster. "3D Numerical Modeling of Steel Corrosion in Concrete Structures." *Corrosion Science*. Vol. 53. pp. 4,166–4,177. 2011.

Pabalan, R.T., L. Yang, K.-T. Chiang. "Boric Acid Degradation of Reinforced Concrete." San Antonio, Texas: Center for Nuclear Waste Regulatory Analyses. 2011.

Pabalan, R. and K. Chiang. "Experimental Study and Reactive Transport Modeling of Boric Acid Leaching of Concrete." Workshop on Long-Term Performance of Cementitious Barriers and Reinforced Concrete in Nuclear Power Plants and Radioactive Waste Storage and Disposal. Cadarache, France, November 12–15, 2012. Gif sur Yvette, France: Laboratory of Concrete and Clay Behaviour Studies. 2012.

Pabalan, R.T., F.P. Glasser, D.A. Pickett, G.R. Walter, S. Biswas, M.R. Juckett, L.M. Sabido, J.L. Myers. "Review of Literature and Assessment of Factors Relevant to Performance of Grouted Systems for Radioactive Waste Disposal." San Antonio, Texas: Center for Nuclear Waste Regulatory Analyses. 2009.

Rothstein, D., J.J. Thomas, B.J. Christensen, and H.M. Jennings. "Solubility Behavior of Ca-, S-, Al-, and Si-Bearing Solid Phases in Portland Cement Pore Solutions as a Function of Hydration Time." *Cement and Concrete Research*. Vol. 32. pp. 1,663–1,671. 2002.

Sagüés, A.A., M.A. Pech-Canul and A.K.M Shaid Al-Mansur. "Corrosion Macrocell Behavior of Reinforcing Steel in Partially Submerged Concrete Columns." *Corrosion Science*, Vol. 45. pp. 7–32. 2003.

SNL. "Nuclear Containment Steel Liner Corrosion Workshop: Final Summary and Recommendation Report." SAND2010-8718. ML112150012. Albuquerque, New Mexico: Sandia National Laboratories. 2011.

Uhlig, H.H. *Corrosion and Corrosion Control*. New York: John Wiley & Sons. 1971.

Warkus, J., M. Raupach, and J. Gulikers. "Numerical Modeling of Corrosion—Theoretical Backgrounds." *Materials and Corrosion*. Vol. 57, No. 8. pp. 614–617. 2006.

Weast, R.C. and M.J. Astle, eds. *CRC Handbook of Chemistry and Physics*. Boca Raton, Florida: CRC Press, Inc. 1981.

Witherspoon, P.A., J.S.Y. Wang, K. Iwai, and J.E. Gale. "Validity of Cubic Law for Fluid Flow in a Deformable Rock Fracture." *Water Resources Research*. Vol. 16, No. 60. pp. 1,016–1,024. 1980.

APPENDIX
ALTERNATIVE OXYGEN REDUCTION EQUATIONS

APPENDIX

ALTERNATIVE OXYGEN REDUCTION EQUATIONS

Two solution methods to determine the solution potential were used to estimate the net ionic current in the liner-rebar-concrete system, which rely on different descriptions on the oxygen reduction kinetics. The alternative methods were explored to investigate model uncertainty. Calculated net ionic currents were independent of the approach to describe the oxygen reduction kinetics.

Method 1

The first method is based on the work by Warkus, et al. (2006). Warkus, et al. (2006) proposed the following equation for i_c

$$i_c = \frac{1 - \exp\left(\frac{\ln(10)(\phi - E_{ref})}{\beta_c}\right)}{\frac{1}{i_{pass}} + \frac{\exp\left(\frac{\ln(10)(\phi - E_{ref})}{\beta_c}\right)}{i_{lim}}} \quad [\text{A-1}]$$

where

i_{pass}	—	passive current density (A/cm^2)
E_{ref}	—	reference potential (0 V)
β_c	—	Tafel slope for the cathodic reduction reaction (176.3 mV)
i_{lim}	—	diffusion-limited current density for the oxygen reduction reaction (A/cm^2)

The equation coupling the oxygen flux to the current at the metal cathode, Eq. [2-13] of the report, is not used in Method 1. Instead, the following equation is used to estimate the diffusion-limited current density for the oxygen reduction reaction, i_{lim}

$$i_{lim} = \frac{nFD_{O_2}C_{O_2}^{atm}}{z} \quad [\text{A-2}]$$

where

n	—	number of electrons per molecule of oxygen in the reduction reaction (4)
F	—	Faraday constant (96500 Coul/mol)
D_{O_2}	—	diffusion coefficient of oxygen (cm^2/sec)
$C_{O_2}^{atm}$	—	oxygen concentration in the concrete porewater at the concrete and air interface (mole/cm^3)
z	—	reference distance representing a maximum oxygen penetration depth (cm)

Equation [A-2] is an approximation of the diffusion-limited current density. A more rigorous method to estimate the current density involves calculation of the oxygen concentration gradient at the cathode, which is implemented in Method 2. The calculated gradient of the oxygen concentration replaces $C_{O_2}^{atm}/z$ in Eq. [A-2]. Equation [A-2] is a valid approximation when the diffusion-limited current density exceeds passive current density.

The mass balance equations for oxygen were relaxed, and the oxygen concentration was allowed to become negative in the COMSOL (COMSOL, Inc., 2013) computations. It is noted in Method 2 that mass balance for oxygen is strictly enforced and oxygen concentration is not allowed to become negative. Negative concentration is interpreted as depleted oxygen in Method 1.

Equation [A-1] becomes

$$i_c = \frac{1 - \exp\left(\frac{\ln(10)(\phi - E_{ref})}{\beta_c}\right)}{\frac{1}{i_{pass}} + \frac{\exp\left(\frac{\ln(10)(\phi - E_{ref})}{\beta_c}\right)}{i_{lim}}} \text{ if } i_{lim} \geq i_{pass} \text{ and } C_{O_2} \geq 0 \quad [\text{A-3}]$$

where C_{O_2} denotes the oxygen concentration in the concrete porewater in units of mol/cm³. As stated in Chapter 2 of the main report, the approximated oxygen concentration distribution is calculated by solving the mass conservation equation, in the form of Fick's second law, for the steady state

$$\nabla^2 C_{O_2} = 0 \quad [\text{A-4}]$$

Equation [A-4] is simultaneously solved subjected to the boundary conditions expressed as Eqs. [2-12] and [2-14] of the report.

Method 2

In Method 2 the system of charge balance and mass balance equations in Chapter 2 are solved, without modification. Parameters for the oxygen reduction current were derived using the OLIAnalyzer software (OLISystems, Inc., 2013). Polarization curves for oxygen reduction were computed considering a system with representative concrete porewater, 1 part per million (ppm) oxygen, and pH=11, 12, 12.5. By curve fitting, the oxygen reduction current, as a function of the solution potential, was estimated as

$$i_{O_2} = i_{O_2}^o \exp\left(\frac{\phi - \phi_o}{\beta_c}\right) \frac{C_{O_2}}{C_{O_2}^o} = \overline{i_{O_2}^o} \exp(17.22V^{-1} \phi) \frac{C_{O_2}}{C_{O_2}^o} \quad [\text{A-5}]$$

where

$$\begin{aligned} \frac{\beta_c}{i_{O_2}^o} &= 1/(17.22 V^{-1}) = 0.058 \text{ V} \\ i_{O_2}^o \exp\left(-\frac{\phi_o}{\beta_c}\right) &= 2.53 \mu\text{A}/\text{cm}^2 \\ C_{O_2}^o &= 1 \text{ ppm} \approx 6.15 \times 10^{-5} \frac{\text{mol}}{\text{L}} \end{aligned}$$

The parameter $i_{O_2}^0$ is treated as an uncertain parameter in the analysis, and calibrated to yield results consistent with empirical data. Based on the OLIAnalyzer (OLISystems, Inc., 2013) simulations, the passive current density was computed to be described as

$$i_p = \frac{1}{\frac{1}{8.46 \times 10^{12} \mu A/cm^2 \exp(-49.8V^{-1}\phi)} + \frac{1}{i_{pass}}} \quad [A-6]$$

The potential dependence is only relevant at a solution potential around $\phi = 600$ mV_{SHE}. The passive steel is expected to be polarized at a much lower potential, on the order of 100 mV_{SHE}. At such potential, i_p is approximated as a constant

$$i_p = i_{pass} \quad [A-7]$$

The value of i_{pass} inferred from the OLIAnalyzer simulations is 0.1 $\mu A/cm^2$. However, i_{pass} is treated as an uncertain parameter, with a value calibrated to be consistent with experimental data. Passive currents of iron in concrete on the order of 0.01 $\mu A/cm^2$ are commonly reported in the literature.

Charge Transfer Resistance

Change transfer resistance at the cathode was estimated to compare to electrolyte resistance to charge flow. The charge transfer resistance is defined according to the following equation

$$\frac{1}{R_{ct}} = \int \frac{\partial i_c}{\partial \phi} dA_{cathode} \quad [A-8]$$

where R_{ct} denotes the charge transfer resistance in units of Ω and $A_{cathode}$ denotes surface area of the cathode.

From Eq. [A-1]

$$\frac{\partial i_c}{\partial \phi} = \frac{\exp\left(\frac{\ln(10)(\phi - E_{ref})}{\beta_c}\right) \times \frac{\ln(10)}{\beta_c}}{\frac{1}{i_{pass}} + \frac{\exp\left(\frac{\ln(10)(\phi - E_{ref})}{\beta_c}\right)}{i_{lim}}} \left[\frac{i_c}{i_{lim}} - 1 \right] \text{ if } i_{lim} \geq i_{pass} \quad [A-9]$$

The charge transfer resistance is obtained by integrating Eq. [A-9] along the rebar surfaces according to Eq. [A-8]. Using a diffusion coefficient of 10^{-5} cm²/sec, and the solution potential distribution, ϕ , associated with a range of driving potentials ($\Delta E=100$ to 500 mV), and a concrete ionic resistivity $\rho=10$ k Ω -cm, integrating over the rebar surfaces yields a charge transfer resistance of approximately 1.4 Ω . This value is much smaller than the ohmic resistance of 250 Ω estimated for an anode with a 10-cm [3.9-in] radius. It is therefore concluded that charge transfer resistance has a minor influence on the net ionic current in the system.

References

COMSOL, Inc. "COMSOL Multiphysics[®]." Burlington, Massachusetts: COMSOL, Inc. 2013. <<http://www.comsol.com/>> (March 8, 2013).

OLISystems, Inc. "OLIAnalyzer Studio." Morris Plains, New Jersey: OLISystems, Inc. 2013 <<http://www.olisystems.com/new-streamanalyzer.shtml>> (March 18, 2013).

Warkus, J. M. Raupach and J. Gulikers. "Numerical Modeling of Corrosion—Theoretical Backgrounds." *Materials and Corrosion*. Vol. 57, No. 8. pp. 614–617. 2006.